

1 **Progressive weakening within the overriding plate during dual inward dipping subduction**

2 Zhibin Lei¹, J. H. Davies¹

3 ¹School of Earth and Environmental Sciences, Cardiff University, Cardiff, CF10 3AT, UK

4 *Correspondence to:* Zhibin Lei (leiz2@cardiff.ac.uk)

5 **Abstract**

6 Dual inward dipping subduction often produces complex deformation patterns in the overriding
7 plate. However, the geodynamic process of how dual inward dipping subduction relates to this
8 deformation remains unclear, as previous investigation all applied a compositional or Newtonian
9 rheology. Here we apply a composite viscosity, dependent on multiple parameters, e.g.,
10 temperature, pressure, strain rate etc., in 2-D thermo-mechanical numerical modelling to
11 investigate how dual inward dipping subduction modifies the rheological structure of the overriding
12 plate. Three variables are investigated to understand what controls the maximum degree of
13 weakening in the overriding plate. We find that reducing the initial length or thickness of the
14 overriding plate and increasing the initial thickness of the subducting plate can enhance the
15 viscosity reduction within the overriding plate during subduction. The progressive weakening can
16 result in a variety of stretching states ranging from 1) little or no lithosphere thinning and extension,
17 to 2) limited thermal lithosphere thinning, and 3) localised rifting followed by spreading extension.
18 Compared with single sided subduction, dual inward dipping subduction further reduces the
19 magnitude of viscosity of the overriding plate. It does this by creating a dynamic fixed boundary
20 condition for the overriding plate and forming a stronger upwelling mantle flow which induces
21 progressive weakening in the overriding plate. Investigation on the evolution of the dominant

22 deformation mechanisms shows that dislocation and yielding contribute most to viscosity reduction,
23 which can lead to rifting and spreading extension in the overriding plate. The progressive
24 weakening is mainly driven by the ever-increasing strain rate, which is also a precondition for
25 initiating thermal weakening, strain localisation, lithosphere thinning and formation of new plate
26 boundaries.

27 **Keywords:** dual inward dipping subduction; composite viscosity; strain localisation; feedback
28 weakening; numerical modelling.

29 **Highlights:**

30 1. Investigate dual inward dipping subduction models implementing composite rheology

31 2. Self-consistently forms a fixed boundary condition and strong convective mantle flow

32 3. Yielding and dislocation creep are the dominant extensional deformation mechanisms

33 4. Strain rate-induced weakening plays a dominant role in initiating viscosity reduction

34 **1. Introduction**

35 Subduction can pose a fundamental tectonic overprint on the overriding plate by generating a
36 volcanic arc (Perfit et al., 1980; Straub et al., 2020), back-arc basin (Uyeda, 1981), orogeny
37 (Faccenna et al., 2021), or even continental breakup (Dal Zilio et al., 2018). Most subduction zones
38 involve only one subducting slab. Here we consider multiple subducting slabs, in particular dual
39 inward dipping subduction. Dual inward dipping subduction, or bi-vergent subduction occurs when
40 the overriding plate is decoupled with two subducting slabs dipping towards each other. It is one of
41 the four most commonly described subduction zones with multiple slabs, i.e., inward-dipping, same-
42 dip, outward-dipping and oppositely dipping adjacent subduction zones (Holt et al., 2017; Király et
43 al., 2021).

44 Dual inward dipping subduction zones are found in areas which exhibit complex geodynamic
45 processes in their geological history. Seismic tomography shows that dual inward dipping
46 subduction exists at the Caribbean plate between the Cocos slab and Lesser-Antilles subduction
47 zone (Van Benthem et al., 2013), and in South-East Asia between the Philippine and the Sumatra
48 subduction (Hall and Spakman, 2015; Huang et al., 2015; Maruyama et al., 2007). In combination
49 with seismic tomography, recent plate reconstructions have made it more evident that dual inward
50 dipping subduction could have existed in some regions in the past (Faccenna et al., 2010; Hall and
51 Spakman, 2015) constrained by suture zone petrology demonstrating the existence of paleo-
52 subduction. A good example is the North China Craton. Suture zone studies reveal that multiple
53 inward dipping subduction may have surrounded the North China Craton from Early Paleozoic to
54 Tertiary (Santosh, 2010; Windley et al., 2010).

55 Global strain rate map (Kreemer et al., 2014) shows that high strain rate regions in the overriding
56 plate is often wider and spatially more complex in multiple slab subduction zones, including the
57 dual inward dipping subduction cases. Besides, crustal scale seismic surveys in the Caribbean Sea
58 has found a good amount of extensional basins spreading widely across the overriding plate since
59 the establishment of dual inward dipping subduction at ~60 Ma (e.g. Boschman et al., 2014;
60 Braszus et al., 2021). Despite these observations, the role dual inward dipping subduction may
61 play to form the high strain rate region, or sedimentary basins remains unclear.

62 Numerical investigations have been conducted to understand the dynamics of dual inward dipping
63 subduction. Research shows that the initial slab dip of the subducting plate affects the upper mantle
64 dynamic pressure between the convergent slabs and stress state within the overriding plate (Holt
65 et al., 2017). Varying the distance between the trenches, convergence rate, and asymmetry of
66 subducting plates can alter the topography of the overriding plate (Dasgupta and Mandal, 2018).
67 The thickness of the plates and the lithosphere to asthenosphere viscosity ratio are all tested to
68 investigate their effect on the slab geometry and the magnitude of mantle upwelling flow underlying
69 the overriding plate (Lyu et al., 2019).

70 These pioneering investigations show that dual inward dipping subduction can generate a variety
71 of upper mantle flow patterns which regulate the stress state and topography of the overriding plate.
72 However, previous models all applied a simplified constant viscosity or Newtonian rheology for both
73 plates and convective mantle flow, i.e., the viscosity is neither temperature nor stress-dependent.
74 Mineral deformation experiments indicate that viscosity varies as a function of multiple parameters,
75 e.g., temperature, pressure, stress, strain rate etc. (Bürgmann and Dresen, 2008; Burov, 2011;

76 Hirth and Kohlstedt, 2003; Karato, 2010; Lynch and Morgan, 1987). Thus, previous dual inward
77 dipping subduction models with simplified rheology were unable to fully reflect the weakening
78 process, e.g., high strain rate in the back-arc region, due to slab rollback and induced mantle wedge
79 flow.

80 Single sided subduction models incorporating composite rheology, e.g., dislocation creep, diffusion
81 creep, yielding etc., has improved our understanding of subduction's impact upon the overriding
82 plate (e.g., Alsaif et al., 2020; Čížková and Bina, 2013; Garel et al., 2014; Schliffke et al., 2022;
83 Suchoy et al., 2021). It has not been investigated before, to the best of our knowledge, in terms of
84 which rheology law dominates the weakening process observed in the overriding plate nor how
85 different deformation mechanisms interplay with each other during subduction.

86 In this research, a series of 2-D thermo-mechanical models incorporating composite rheology laws
87 are run to investigate how dual inward dipping subduction differs from single sided subduction in
88 deforming the overriding plate. We also identify the dominant deformation mechanism that induces
89 progressive weakening and investigate the interplay among different deformation mechanisms
90 applied.

91 **2. Methods**

92 We ran the thermally-driven dual inward dipping subduction models using the code Fluidity (Davies
93 et al., 2011; Kramer et al., 2012), a finite-element control-volume computational modelling
94 framework, with an adaptive mesh that is set up to capture evolving changes of velocity,
95 temperature, viscosity etc., with a maximum resolution of 0.4 km in this research.

96 **2.1 Governing equations and rheology setup**

97 Under the Boussinesq approximation (McKenzie et al., 1974), the equations governing thermally
 98 driven subduction process are derived from conservation of mass, momentum, and energy, for an
 99 incompressible Stokes flow

$$\partial_i u_i = 0, \quad (1)$$

$$\partial_i \sigma_{ij} = -\Delta \rho g_j, \quad (2)$$

$$\frac{\partial T}{\partial t} + u_i \partial_i T = \kappa \partial_i^2 T, \quad (3)$$

100 in which u , g , σ , T , κ are the velocity, gravity, stress, temperature, and thermal diffusivity,
 101 respectively (Table 1). In particular, the full stress tensor σ_{ij} consists of deviatoric and lithostatic
 102 components via

$$\sigma_{ij} = \tau_{ij} - p \delta_{ij}, \quad (4)$$

103 where τ_{ij} represents the deviatoric stress tensor, p the dynamic pressure, and δ_{ij} the Kronecker
 104 delta function.

105 The deviatoric stress tensor and strain rate tensor $\dot{\epsilon}_{ij}$ are related according to

$$\tau_{ij} = 2\mu \dot{\epsilon}_{ij} = \mu(\partial_j u_i + \partial_i u_j), \quad (5)$$

106 with μ the viscosity. The density difference due to temperature is defined as

$$\Delta\rho = -\alpha\rho_s(T - T_s), \quad (6)$$

107 where α is the coefficient of thermal expansion, ρ_s is the reference density at the surface
108 temperature T_s (Table 1).

Table 1. Key parameters used in this research.

| Quantity | Symbol | Units | Value |
|---|----------------|---------------------|--|
| Gravity | g | $m s^{-2}$ | 9.8 |
| Gas constant | R | $J K^{-1} mol^{-1}$ | 8.3145 |
| Mantle geothermal gradient | G | $K km^{-1}$ | 0.5 (UM) 0.3 (LM) |
| Thermal expansivity coefficient | α | K^{-1} | 3×10^{-5} |
| Thermal diffusivity | κ | $m^2 s^{-1}$ | 10^{-6} |
| Reference density | ρ_s | $kg m^{-3}$ | 3300 |
| Cold, surface temperature | T_s | K | 273 |
| Hot, mantle temperature | T_m | K | 1573 |
| Maximum viscosity | μ_{max} | $Pa \cdot s$ | 10^{25} |
| Minimum viscosity | μ_{min} | $Pa \cdot s$ | 10^{18} |
| Diffusion Creep^a | | | |
| Activation energy | E | $kJ mol^{-1}$ | 300 (UM) 200 (LM) |
| Activation volume | V | $cm^3 mol^{-1}$ | 4 (UM) 1.5 (LM) |
| Prefactor | A | $Pa^{-n} s^{-1}$ | 3.0×10^{-11} (UM) 6.0×10^{-17} (LM) |
| | n | | 1 |
| Dislocation Creep (UM)^b | | | |
| Activation energy | E | $kJ mol^{-1}$ | 540 |
| Activation volume | V | $cm^3 mol^{-1}$ | 12 |
| Prefactor | A | $Pa^{-n} s^{-1}$ | 5.0×10^{-16} |
| | n | | 3.5 |
| Peierls Creep (UM)^c | | | |
| Activation energy | E | $kJ mol^{-1}$ | 540 |
| Activation volume | V | $cm^3 mol^{-1}$ | 10 |
| Prefactor | A | $Pa^{-n} s^{-1}$ | 10^{-150} |
| | n | | 20 |
| Yield Strength Law^d | | | |
| Surface yield strength | τ_0 | MPa | 2 |
| Friction coefficient | f_c | | 0.2 |
| | $f_{c,weak}$ | | 0.02 (weak layer) |
| Maximum yield strength | $\tau_{y,max}$ | MPa | 10,000 |

^a The rheology parameter of diffusion creep is guided by previous mineral deformation experiments (Hirth and Kohlstedt, 2003, 1995a; Ranalli, 1995). The UM and LM stands for “upper mantle” and “lower mantle,” respectively. ^b The activation parameters and stress-dependent exponent used for dislocation creep are in agreement with previous mineral deformation experiments (Hirth and Kohlstedt, 1995b). ^c The parameterisation (based on Kameyama et al., 1999) makes Peierls creep tend to be weaker than yielding in the upper mantle, thus enabling trench retreat and creating richer slab morphology in the upper mantle (Garel et al., 2014). ^d A very high maximum yield strength value is used here to ensure that yielding only dominates at the depth of crustal scale. A friction coefficient of 0.2 is following numerical models (Garel et al., 2014; Gülcher et al., 2020), and it is intermediate between lower values of previous subduction models (Crameri et al., 2012; Di Giuseppe et al., 2008) and the actual friction coefficient of the Byerlee law (Byerlee, 1978).

119 The key rheology difference of the model setup with previous dual inward dipping subduction
 120 models (Dasgupta and Mandal, 2018; Holt et al., 2017; Lyu et al., 2019) is that the magnitude of
 121 viscosity throughout the model can self-consistently evolve during subduction. The governing
 122 rheological laws are identical throughout the model domain, though the rheology parameters we
 123 use differ to match different deformation mechanisms potentially dominating at different depths in
 124 the Earth. In detail, a uniform composite viscosity is used to take account of four deformation
 125 mechanisms under different temperature-pressure conditions: diffusion creep, dislocation creep,
 126 Peierls mechanism, and yielding (Garel et al., 2014). The effective composite viscosity in the
 127 computational domain is given by

$$\mu = \left(\frac{1}{\mu_{diff}} + \frac{1}{\mu_{disl}} + \frac{1}{\mu_P} + \frac{1}{\mu_y} \right)^{-1}, \quad (7)$$

128 where μ_{diff} , μ_{disl} , μ_y define the creep viscosity following

$$\mu_{diff/disl/P} = A^{-\frac{1}{n}} \exp \left(\frac{E + PV}{nRT_r} \right) \dot{\varepsilon}_{II}^{\frac{1-n}{n}}, \quad (8)$$

129 in which A is a prefactor, n the stress component, E the activation energy, P the lithostatic
 130 pressure, V the activation volume, R the gas constant, T_r the temperature obtained by adding
 131 an adiabatic gradient of 0.5 K/km in the upper mantle and 0.3 K/km in the lower mantle to the
 132 Boussinesq solution (Fowler, 2005), $\dot{\varepsilon}_{II}$ the second invariant of the strain rate tensor. Note that in
 133 the lower mantle only diffusion creep applies and the lower mantle is 30 times more viscous than
 134 the upper mantle. While the fourth deformation mechanism, yielding, is defined by a brittle-failure
 135 type yield-stress law as

$$\mu_y = \frac{\tau_y}{2\dot{\varepsilon}_{II}}, \quad (9)$$

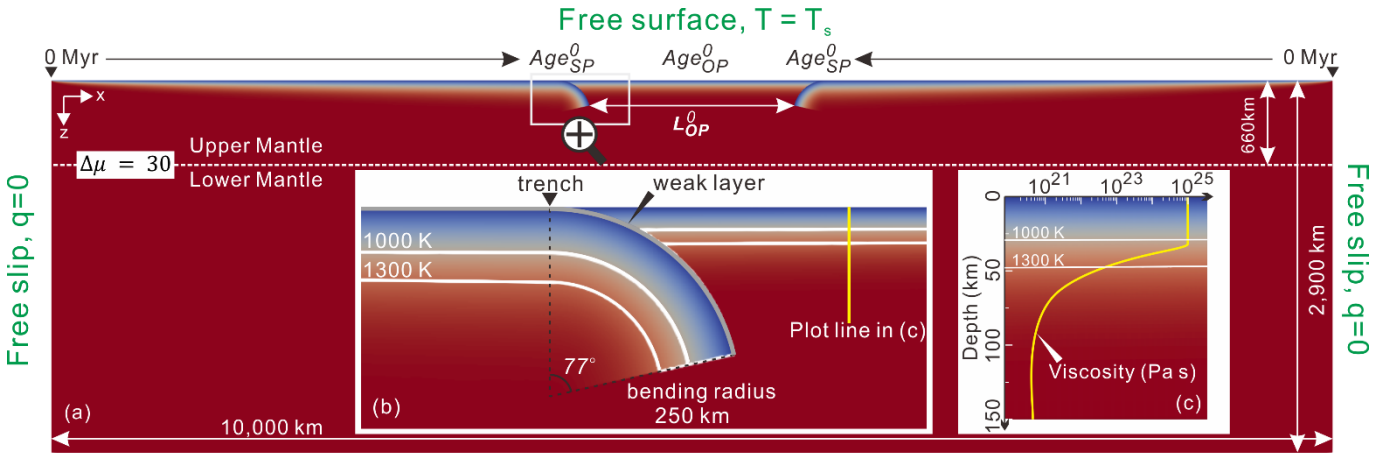
136 with μ_y the yielding viscosity and τ_y the yield strength. τ_y is determined by

$$\tau_y = \min(\tau_0 + f_c P, \tau_{y,max}), \quad (10)$$

137 with τ_0 the surface yield strength, f_c the friction coefficient, P the lithostatic pressure, and
138 $\tau_{y,max}$ the maximum yield strength (Table 1).

139 **2.2 Model setup**

140 The computational domain is 10,000 km by 2,900 km, with x (width) coordinates and z (depth)
141 coordinates extending from the surface to the bottom of the lower mantle (Figure 1). Such a wide
142 domain reduces the influence of side and bottom boundary conditions (Chertova et al., 2012). The
143 thermal boundary conditions at the surface and bottom are defined by two isothermal values: $T =$
144 T_s and $T = T_m$ for surface and base of lower mantle respectively, while the sidewalls are insulating.
145 As for mechanical boundary conditions, a free-surface is applied at the top boundary to facilitate
146 trench mobility, and create more accurate topography and lithosphere stress state, while the other
147 boundaries are free-slip.



Free surface, $T = T_s$

148

149

150

151

152

153

154

155

156

157

158

159

160

161

162

163

164

165

166

167

168

169

170

171

172

173

174

175

176

177

178

179

180

181

182

183

184

185

186

187

188

189

190

191

192

193

194

195

196

197

198

199

200

201

202

203

204

205

206

207

208

209

210

211

212

213

214

215

216

217

218

219

220

221

222

223

224

225

226

227

228

229

230

231

232

233

234

235

236

237

238

239

240

241

242

243

244

245

246

247

248

249

250

251

252

253

254

255

256

257

258

259

260

261

262

263

264

265

266

267

268

269

270

271

272

273

274

275

276

277

278

279

280

281

282

283

284

285

286

287

288

289

290

291

292

293

294

295

296

297

298

299

300

301

302

303

304

305

306

307

308

309

310

311

312

313

314

315

316

317

318

319

320

321

322

323

324

325

326

327

328

329

330

331

332

333

334

335

336

337

338

339

340

341

342

343

344

345

346

347

348

349

350

351

352

353

354

355

356

357

358

359

360

361

362

363

364

365

366

367

368

369

370

371

372

373

374

375

376

377

378

379

380

381

382

383

384

385

386

387

388

389

390

391

392

393

394

395

396

397

398

399

400

401

402

403

404

405

406

407

408

409

410

411

412

413

414

415

416

417

418

419

420

421

422

423

424

425

426

427

428

429

430

166 thermal diffusivity. All parameters are listed in Table 1. The whole overriding plate is set up with a
167 constant age. Thus, the thermal structure within the overriding plate is laterally homogeneous. The
168 bottom of the thermal lithosphere is defined as the isotherm of 1300 K, where the temperature
169 gradient starts to drop quickly (Garel and Thoraval, 2021). The initial thickness of the subducting
170 plate (H_{SP}^0) and overriding plate (H_{OP}^0) can be calculated using

$$H_{Plate}^0 = \text{erfinv}((T_{1300K} - T_s)/(T_m - T_s)) * 2 * \sqrt{\kappa * \text{Age}_{Plate}^0(x)}, \quad (12)$$

171 where H_{Plate}^0 is the initial thickness of the plate thermal lithosphere and erfinv is the inverse error
172 function.

173 The free surface boundary condition together with the mid-ocean ridge setup allows the subducting
174 slabs, the overriding plate and therefore the trench to move freely as subduction evolves. To initiate
175 self-driven subduction without implementing external forces, the subducting plate is set up with a
176 bend into the mantle and an 8 km thick low-viscosity decoupling layer on the top. This weak layer
177 has the same rheology as the rest of the domain, other than its maximum viscosity is 10^{20} Pa s,
178 and its friction coefficient is 0.02 (i.e., an order of magnitude lower). The initial bending radius is
179 250 km and initially the slab bends over 77 degrees from the trench (Figure 1).

180 2.3 Model variables

181 Three variables are investigated here: the initial length of the overriding plate (L_{OP}^0), the initial
182 thickness of the subducting plate (H_{SP}^0) and overriding plate (H_{OP}^0) (Table 2). These are parameters
183 also varied in previous research and therefore will allow easier comparison. H_{SP}^0 and H_{OP}^0 are

184 dependent on plate age and calculated using Equation (12). The magnitude of L_{OP}^0 that has been
 185 tested in previous models ranges from 500 km to 4000 km (Dasgupta and Mandal, 2018; Holt et
 186 al., 2017; Lyu et al., 2019), and the result shows that L_{OP}^0 greater than 2500 km has little impact
 187 on the result (Lyu et al., 2019). Here L_{OP}^0 is tested in the range from 500 km to 1600 km. The values
 188 of H_{SP}^0 and H_{OP}^0 that has been tested before ranges from 75-125 km and 75-150 km separately
 189 and those models suggest that H_{SP}^0 is more important in deciding the magnitude of upwelling
 190 mantle flow than H_{OP}^0 (Lyu et al., 2019). So the range of H_{SP}^0 is extended to 94-141 km (90-200
 191 Ma, Table 2) while the range of H_{OP}^0 is narrowed down to 67-100 km (45-100 Ma).

192 Table 2. List of model setup.

| Model name | L_{OP}^0 (km) | H_{SP}^0 (km) | H_{OP}^0 (km) | Age_{SP}^0 (Ma) | Age_{OP}^0 (Ma) |
|------------------------------|-----------------|-----------------|-----------------|-------------------|-------------------|
| $H_{SP}^0 = 94 \text{ km}$ | 500 | 94 | 67 | 90 | 45 |
| $H_{SP}^0 = 100 \text{ km}$ | 500 | 100 | 67 | 100 | 45 |
| $H_{SP}^0 = 111 \text{ km}$ | 500 | 111 | 67 | 125 | 45 |
| $H_{SP}^0 = 122 \text{ km}$ | 500 | 122 | 67 | 150 | 45 |
| $H_{SP}^0 = 141 \text{ km}$ | 500 | 141 | 67 | 200 | 45 |
| $H_{OP}^0 = 67 \text{ km}$ | 500 | 141 | 67 | 200 | 45 |
| $H_{OP}^0 = 70 \text{ km}$ | 500 | 141 | 70 | 200 | 50 |
| $H_{OP}^0 = 74 \text{ km}$ | 500 | 141 | 74 | 200 | 55 |
| $H_{OP}^0 = 77 \text{ km}$ | 500 | 141 | 77 | 200 | 60 |
| $H_{OP}^0 = 100 \text{ km}$ | 500 | 141 | 100 | 200 | 100 |
| $L_{OP}^0 = 500 \text{ km}$ | 500 | 141 | 67 | 200 | 45 |
| $L_{OP}^0 = 600 \text{ km}$ | 600 | 141 | 67 | 200 | 45 |
| $L_{OP}^0 = 700 \text{ km}$ | 700 | 141 | 67 | 200 | 45 |
| $L_{OP}^0 = 800 \text{ km}$ | 800 | 141 | 67 | 200 | 45 |
| $L_{OP}^0 = 1000 \text{ km}$ | 1000 | 141 | 67 | 200 | 45 |
| $L_{OP}^0 = 1200 \text{ km}$ | 1200 | 141 | 67 | 200 | 45 |
| $L_{OP}^0 = 1600 \text{ km}$ | 1600 | 141 | 67 | 200 | 45 |

193 Models are named with the variable tested, e.g., $H_{SP}^0 = 94 \text{ km}$ and $H_{SP}^0 = 122 \text{ km}$ corresponds to the initial subducting plate
 194 thickness of 94 km and 122 km separately, while the initial overriding plate length and thickness in both models remain the same as
 195 500 km and 67 km.

196 3. Results

197 3.1 Varying viscosity in an evolving model: an example

198 The thermal-mechanical model setup of this research enables self-consistent subduction. Similar
199 to the self-consistent single subduction numerical and analogue models, subduction initiates as
200 negative buoyancy pulls the slab to sink into the deeper mantle, followed by a second stage when
201 slab starts to interact with the lower mantle (e.g., Capitanio et al., 2010; Gerya et al., 2008; Schellart
202 and Moresi, 2013). We next describe in detail the dynamic evolution of dual inward dipping
203 subduction for the model ' $L_{OP}^0 = 1200 \text{ km}$ '.

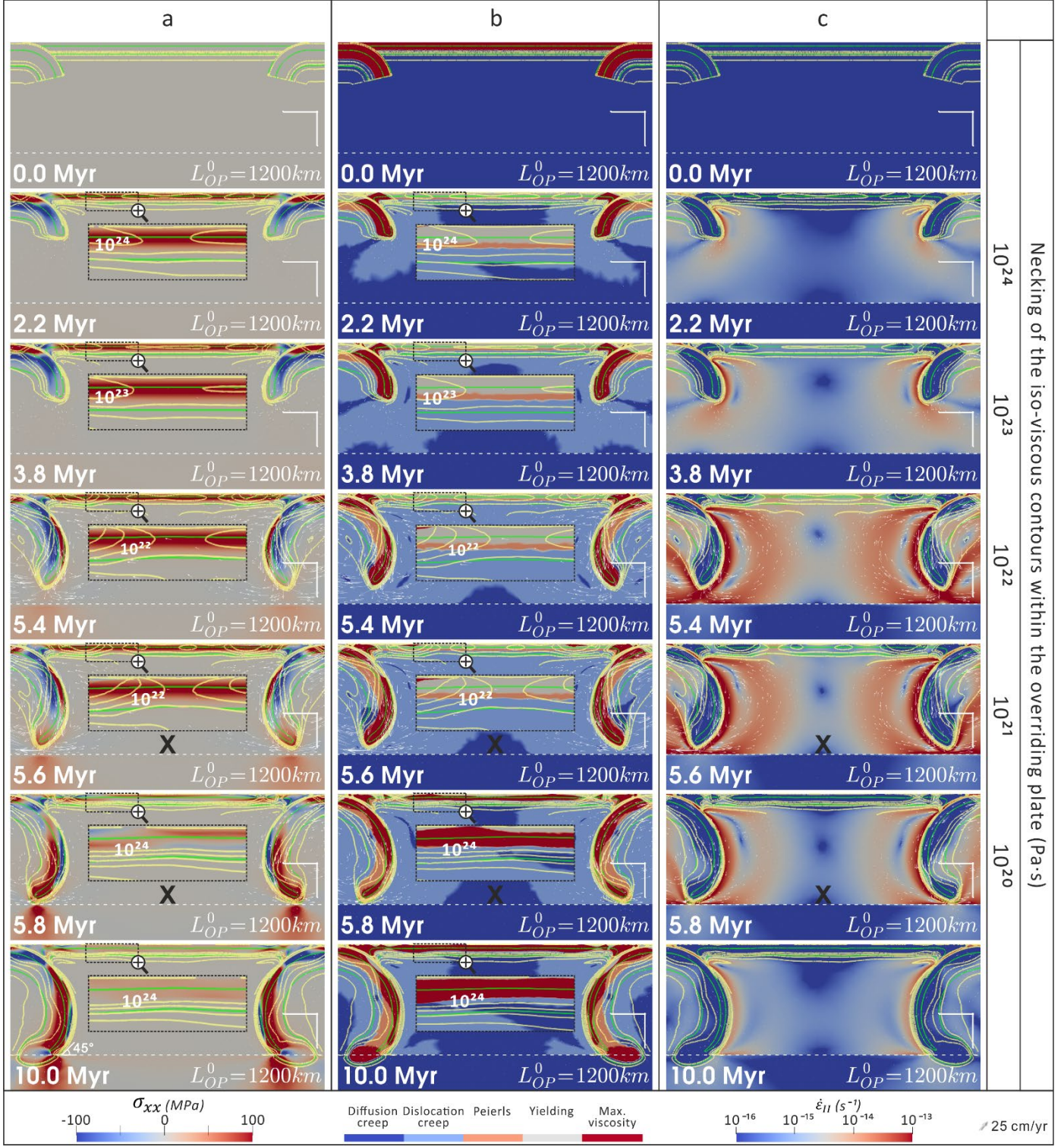
204 **3.1.1 Subduction through the upper mantle**

205 When slabs subduct through the upper mantle, symmetric subduction develops about the midline
206 of the overriding plate (~5000km away from the side boundaries). As more slab is pulled into the
207 mantle, the negative buoyancy grows gradually. It takes ~5.8 Myr before the slab starts to interact
208 with the lower mantle (Figure 2).

209 Convective mantle wedge flow is generated as the subducting slab bends and sinks in the upper
210 mantle. The size of the convective cell grows with time and forms a crescent shape as wide as
211 ~500 km before the slab reaches the depth of lower mantle. The convective cell is composed of a
212 narrow downwelling flow coupling close to the sinking slab and a wide upwelling flow further away.
213 The upwelling flow fades gradually as its distance away from the subducting slab increases. In the
214 model ' $L_{OP}^0 = 1200 \text{ km}$ ', the two sets of wedge flow have little interaction and can be considered as
215 two separate units. This is because the length of the overriding plate is 1200 km, which is greater
216 than two times the width (~500 km) of a convection cell.

217 The overriding plate exhibits a widespread extensional stress field as a result of continuous

218 subduction and the induced convective mantle wedge flows. Only a limited area close to the
219 interface with the bending slabs develops compression (Figure 2, a). The widespread extensional
220 stress field implies that the overriding plate has an overall stretching tendency. Within the overriding
221 plate, the governing deformation mechanism is spatially layered (Figure 2, b). At depths shallower
222 than 30 km within the overriding plate, yielding (brittle or plastic) deformation dominates. Underlying
223 the yielding layer lies ~10 km thick Peierls creep layer. While for depths from ~40 km to the bottom
224 of the thermal lithosphere deformation is dominated by dislocation creep. High strain rate areas are
225 observed within and underneath the overriding plate (Figure 2, c). The thermal thickness of the
226 overriding plate, defined by the 1300 K isotherm contour, remains nearly constant throughout the
227 simulation.



240 The non-Newtonian rheology laws applied define viscosity as a function of multiple variables, e.g.,
241 temperature, lithostatic pressure, stress, strain rate etc. As subduction initiates, it creates rheology
242 heterogeneities within what initially was a laterally homogeneous overriding plate, allowing part of
243 it to become weaker than other parts. To visualize the variation in lithosphere viscosity, several
244 levels of iso-viscous contours are plotted, e.g., $10^{24}, 10^{23}, 10^{22}, 10^{21} \text{ Pa} \cdot \text{s}$ (Figure 2). Here, the
245 overriding plate weakening is defined as the viscosity reduction process, and the weakening level
246 is defined as the maximum order of viscosity magnitude drop. That is, weakening level 'I', 'II', 'III',
247 'IV' represents that the iso-viscous contour $10^{24}, 10^{23}, 10^{22}, 10^{21} \text{ Pa} \cdot \text{s}$ is necked within the
248 overriding plate respectively. It shows that the homogeneous overriding plate is gradually
249 segmented into three strong cores connected with two low viscosity necking regions. Strain is likely
250 to localise upon these two necking areas and continuously lower the magnitude of viscosity therein.
251 The minimum viscosity achieved in the overriding plate for model ' $L_{OP}^0 = 1200 \text{ km}$ ' is $10^{21}-10^{22} \text{ Pa} \cdot$
252 s (weakening level 'III'). The distance between these two necking regions is $\sim 620 \text{ km}$ (Figure 2, a,
253 3.8Myr). These necking regions match well with the high strain rate areas developed in the
254 overriding plate. The initial result suggests that high strain rate may play an important role in
255 softening the overriding plate during dual inward dipping subduction.

256 **3.1.2 Subduction into the lower mantle**

257 Due to the viscosity jump at transition zone, subduction approaching the lower mantle would
258 experience a short period of deceleration, where mobility of the slab tends to slow down and the
259 induced mantle wedge flow becomes mild. Meanwhile, the necking of the iso-viscous contours is
260 reversed by a cooling and strengthening process within the overriding plate (Figure 2). At the end

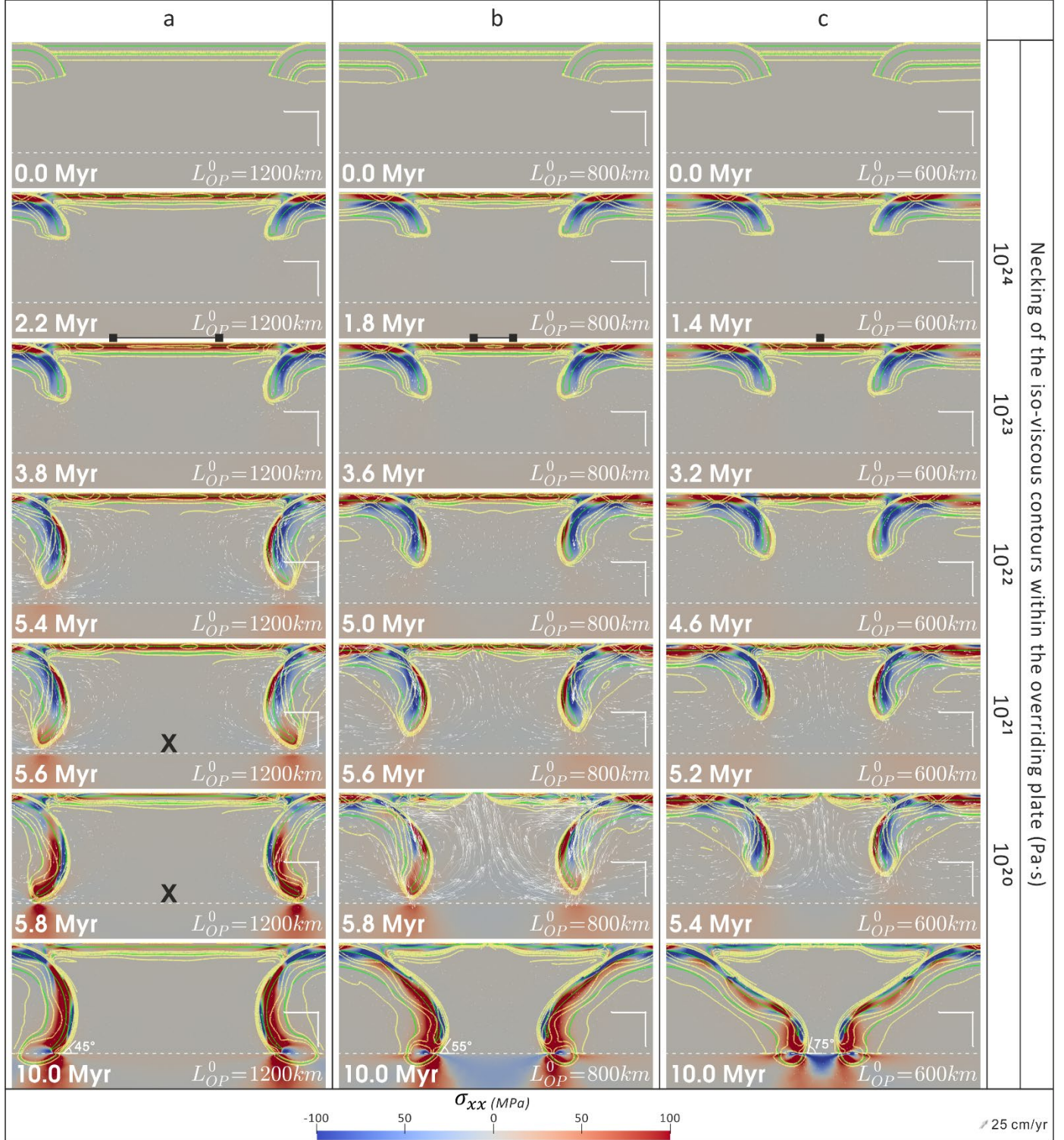
261 of the 10 Myr simulation, the dip between the top of bending slab and the transition zone is ~45°
262 and the total trench retreat is ~100 km.

263 **3.2 Length of the overriding plate**

264 The first series of models investigate decreasing the initial length of the overriding plate (L_{OP}^0) from
265 1600 km to 500 km, while keeping the initial thickness of the subducting and overriding plate as
266 141 km and 67 km separately. As L_{OP}^0 decreases, the two symmetric subducting slabs become
267 closer. The two separate convective mantle wedge flows start to combine with each other and form
268 a stronger joint upwelling flow underneath the overriding plate (Figure 3). Consequently, as L_{OP}^0 is
269 reduced, the two separate necking areas within the overriding plate get closer and merge into a
270 single one in the end. Also as L_{OP}^0 is reduced it takes less time to lower each level of viscosity
271 within the overriding plate. Besides, the progressive weakening process can go further and neck
272 the 10^{21} Pa s iso-viscous contour (weakening level 'IV') when L_{OP}^0 reaches ≤ 800 km, initiating
273 significant lithosphere thinning and even rifting or spreading extension within the overriding plate
274 (Figure 3, b-c). In this paper, we define rifting as a process where the plate's thermal thickness
275 reduces to ~0 km. It is noted that the rifting process in this research does not include melting
276 behaviour. The significant extension usually lasts less than 1 Myr before it gradually stops after the
277 slab reaches the depth of the lower mantle, but it causes substantial changes to the dual inward
278 dipping subduction system. For example, significant slab rollback starts to develop, creating a
279 flattening slab geometry in the upper mantle and steepening dip angle (45° to 75°, Figure 3) at the
280 transition zone depth by the end of the 10 Myr simulation.

281 It is noted that the continuous thinning of the thermal lithosphere only initiates when the iso-viscous

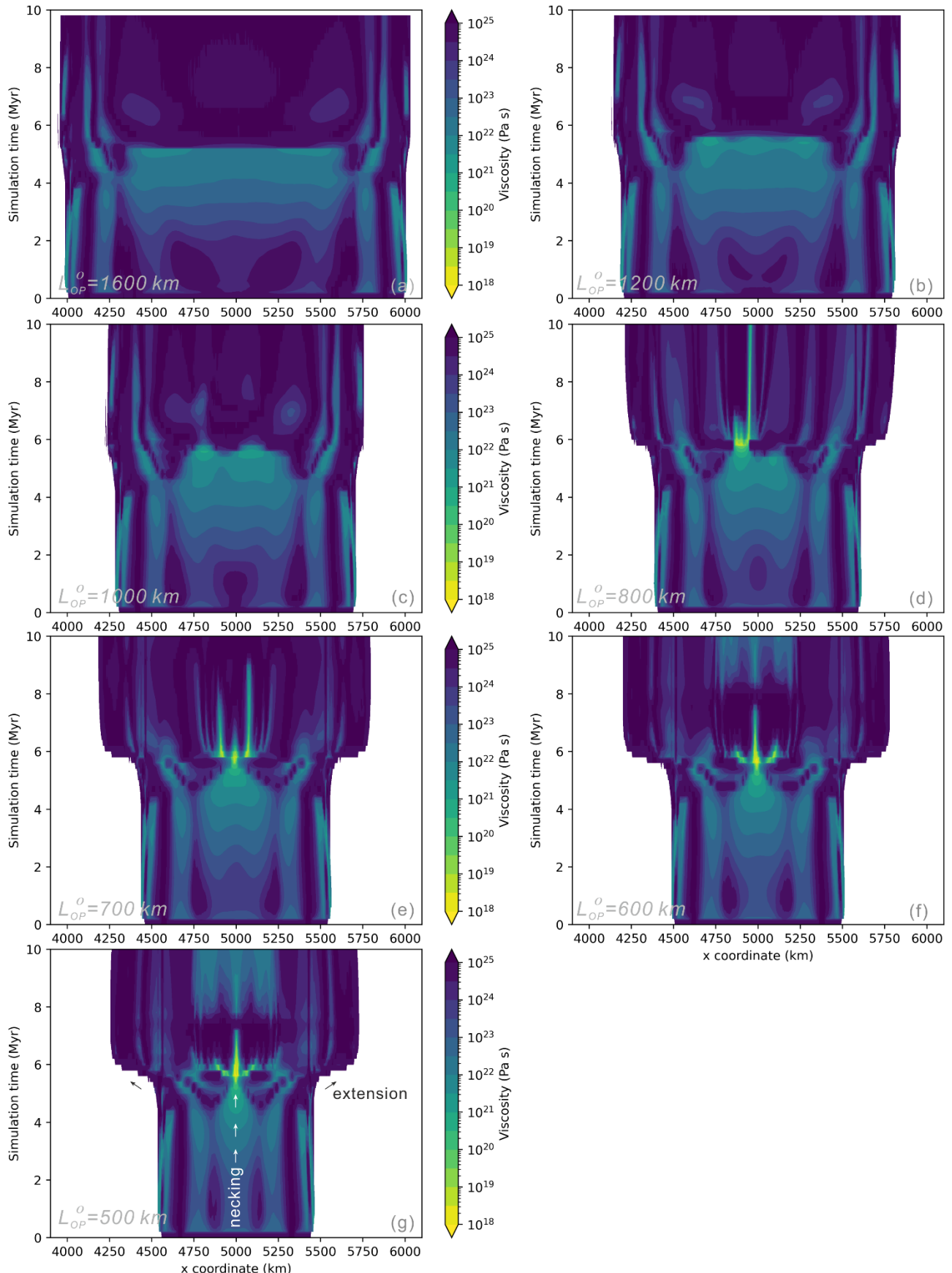
282 contour of $10^{21} \text{ Pa} \cdot \text{s}$ starts to neck, indicating a good correlation of the thermal lithosphere and
283 the rheology boundary layer (usually defined as the depth of $10^{21} \text{ Pa} \cdot \text{s}$) in the model. All models
284 necking $10^{21} \text{ Pa} \cdot \text{s}$ will continue to neck lower magnitudes of viscosity, e.g., $10^{20}, 10^{19} \text{ Pa} \cdot \text{s}$.
285 Simultaneously, the upwelling hot mantle flow can then ascend to fill the thinning region and create
286 a new plate boundary (rifting extension) or even new sea floor (spreading extension) after it
287 ascends to the surface. Thus, the ability to neck $10^{21} \text{ Pa} \cdot \text{s}$ (or not) can be used as a key
288 diagnostic to predict whether a new spreading ridge (new plate boundary) develops within the
289 overriding plate (or just limited thinning).



290
291 Figure 3. Progressive weakening of the overriding plate during dual inward dipping subduction with decreasing length of the
292 overriding plate, (a) model ' $L_{OP}^0 = 1200 \text{ km}$ ', (b) model ' $L_{OP}^0 = 800 \text{ km}$ ', (c) model ' $L_{OP}^0 = 600 \text{ km}$ '. The location of necked regions in
293 the overriding plate are marked with black squares. A detailed explanation of the contours and symbols could be found in the caption
294 of Figure 2.

295 To take a closer look at the extension behaviour within the overriding plate, we plot the evolving
296 magnitude of viscosity at 5km depth (Figure 4). The filled region in the figure represents the
297 overriding plate, therefore its widening represents extension within the overriding plate. As the initial

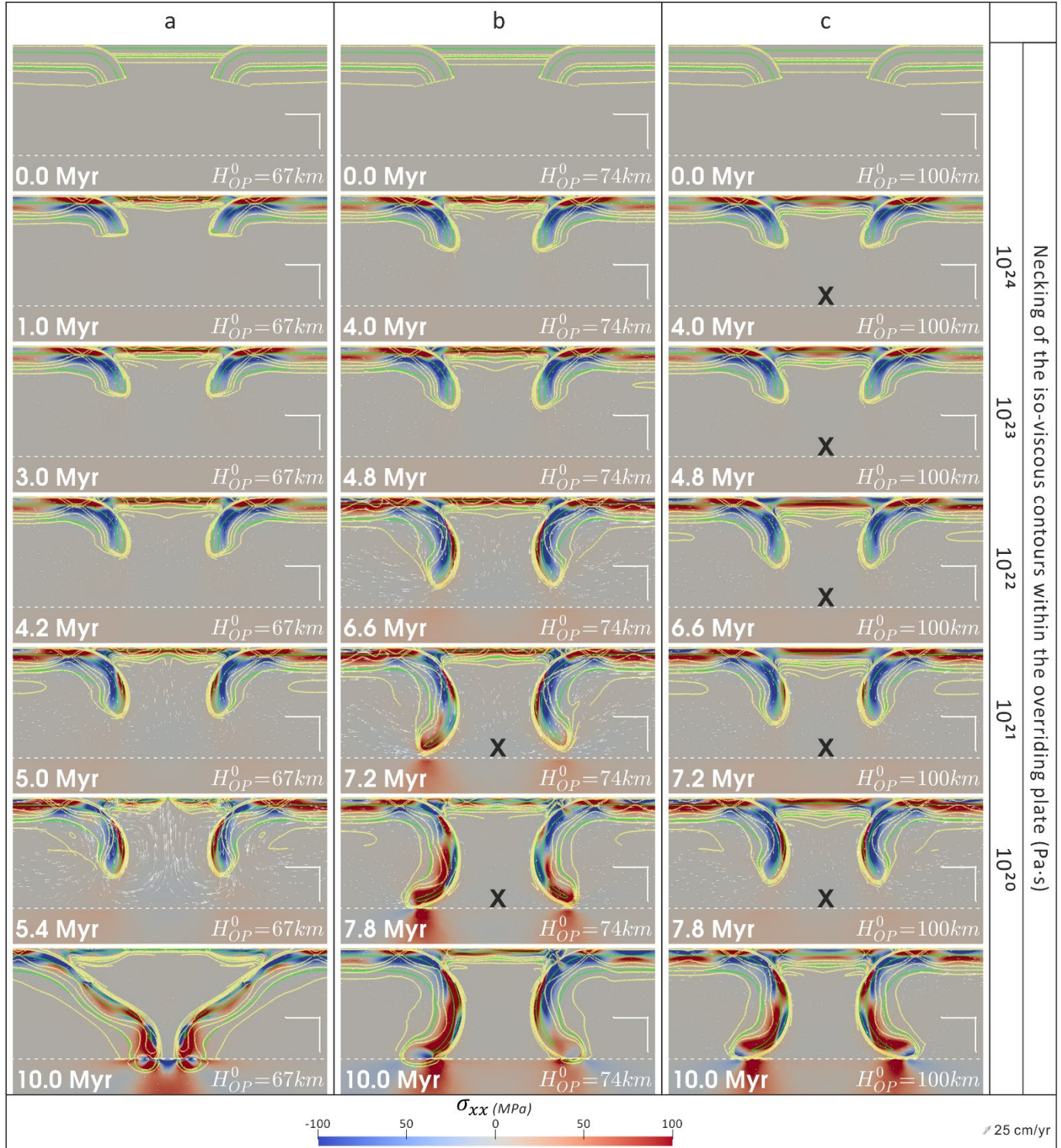
298 length of the overriding plate (L_{OP}^0) decreases from 1600 km to 500 km, the total extension in the
299 10 Myr simulations increases from ~100 km (Figure 4, a-c) to 400-600 km (Figure 4, d-g). In detail,
300 it is noted that extensional behaviour only become observable after the iso-viscous contour of
301 $10^{23} \text{ Pa} \cdot \text{s}$ is necked, i.e., after weakening level ‘II’ is achieved. Extension combining with
302 lithospheric thinning only becomes significant when the iso-viscous contour $10^{21} \text{ Pa} \cdot \text{s}$ is necked,
303 i.e., when weakening level ‘IV’ is achieved. The highest weakening level achieved within the
304 overriding plate increases from ‘II’ ($L_{OP}^0 = 1600 \text{ km}$) to ‘III’ ($L_{OP}^0 = 1000 \text{ km}$) and on to ‘IV’ ($L_{OP}^0 \leq$
305 800 km). During the spreading extension period, a highly centralised spreading centre (Figure 4,
306 d,f-g) is observed in the middle of the overriding plate (Figure 4, d, f-g), while multiple spreading
307 centres are observed to accommodate the extension in model ‘ $L_{OP}^0 = 700 \text{ km}$ ’ (Figure 4, e).



308
309 Figure 4. Temporal evolution of viscosity magnitude along the depth of 5 km within the overriding plate for models with different
310 length of the overriding plate. (a) Model ' $L_{OP}^0 = 1600 \text{ km}$ '. (b) Model ' $L_{OP}^0 = 1200 \text{ km}$ '. (c) Model ' $L_{OP}^0 = 1000 \text{ km}$ '. (d) Model ' $L_{OP}^0 =$
311 800 km '. (e) Model ' $L_{OP}^0 = 700 \text{ km}$ '. (f) Model ' $L_{OP}^0 = 600 \text{ km}$ '. (g) Model ' $L_{OP}^0 = 500 \text{ km}$ '. All models have the same setup of H_{SP}^0
312 (141 km) and H_{OP}^0 (67 km). The edge of the filled contour in the lateral direction represents the interface between the overriding
313 plate and subducting plate. The white arrows display the necking process of the overriding plate.

314 **3.3 Thickness of the overriding plate**

315 The second series of models increase the initial thermal thickness (defined by the 1300 K contour)
316 of the overriding plate (H_{OP}^0) from 67 km to 100 km (Figure 5), while keeping the subducting plate's
317 thickness (H_{SP}^0) and the length of the overriding plate (L_{OP}^0) constant (Table 2). As H_{OP}^0 increases,
318 the maximum weakening level developed within the overriding plate drops from 'IV' ($H_{OP}^0 = 67 \text{ km}$)
319 to 'III' ($H_{OP}^0 = 74 \text{ km}$) and less than 'I' ($H_{OP}^0 = 100 \text{ km}$). The time it takes to lower each order of
320 viscosity magnitude increases, indicating a slower progressive weakening.

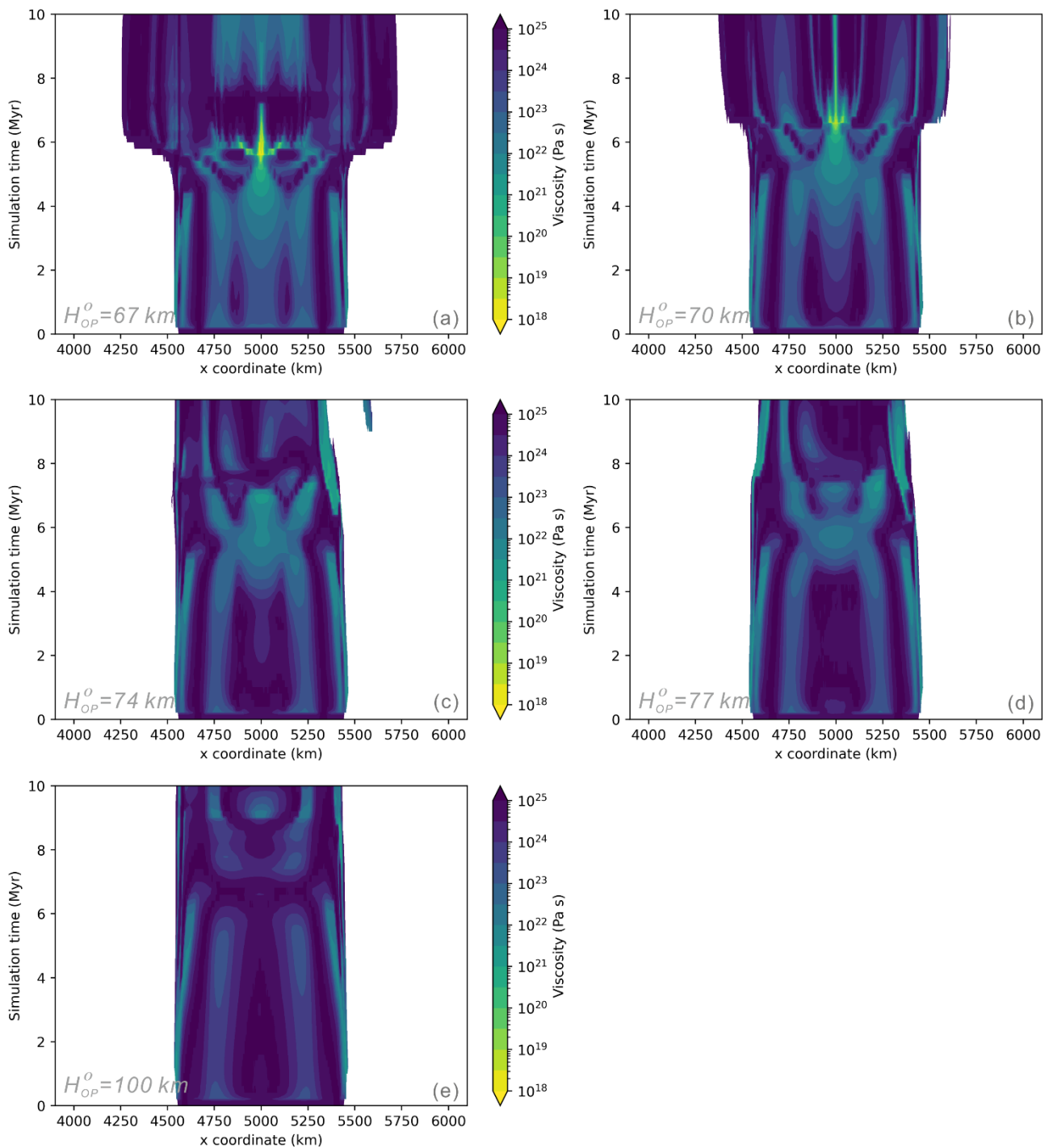


321
322 Figure 5. Progressive weakening, illustrated by visualising the stress σ_{xx} , of the overriding plate during dual inward dipping
323 subduction with increasing thickness of the overriding plate, (a) model ' $H_{OP}^0 = 67 \text{ km}$ ', (b) model ' $H_{OP}^0 = 74 \text{ km}$ ' and (c) model ' $H_{OP}^0 =$
324 100 km '. A detailed explanation of the contours and symbols could be found in the caption of Figure 2.

325 Besides, the total extension decreases from $\sim 600 \text{ km}$ ($H_{OP}^0 = 67 \text{ km}$, Figure 6, a) to $\sim 350 \text{ km}$ ($H_{OP}^0 =$
326 70 km , Figure 6, b) and ultimately to $\sim 0 \text{ km}$ ($H_{OP}^0 = 100 \text{ km}$, Figure 6, c-e). The maximum viscosity
327 reduction in both the primary and secondary necking regions decreases as H_{OP}^0 increases, while

328 the lateral distance away from the trench of necking regions are equal, showing no correlation with

329 H_{OP}^0 .



330

331 Figure 6. Temporal evolution of viscosity along a horizontal line at the depth of 5km in the overriding plate. (a) Model ' $H_{OP}^0 = 67 \text{ km}$ '.
332 (b) Model ' $H_{OP}^0 = 70 \text{ km}$ '. (c) Model ' $H_{OP}^0 = 74 \text{ km}$ '. (d) Model ' $H_{OP}^0 = 77 \text{ km}$ '. (e) Model ' $H_{OP}^0 = 100 \text{ km}$ '. All models have the same
333 H_{SP}^0 (141 km) and L_{OP}^0 (500 km). The edge of the contour filling in the lateral direction represents the interface between the
334 overriding plate and subducting plate.

335 To investigate the details of the progressive weakening in the necking region, 5 diagnostics are
 336 evaluated along the vertical slice in the middle of the overriding plate (5000 km away from both
 337 side boundaries). This is where the necking belt develops in models with L_{OP}^0 of 500 km. The
 338 diagnostics are integrated along the vertical slice and then divided by the thickness of the plate
 339 (Equation (13)),

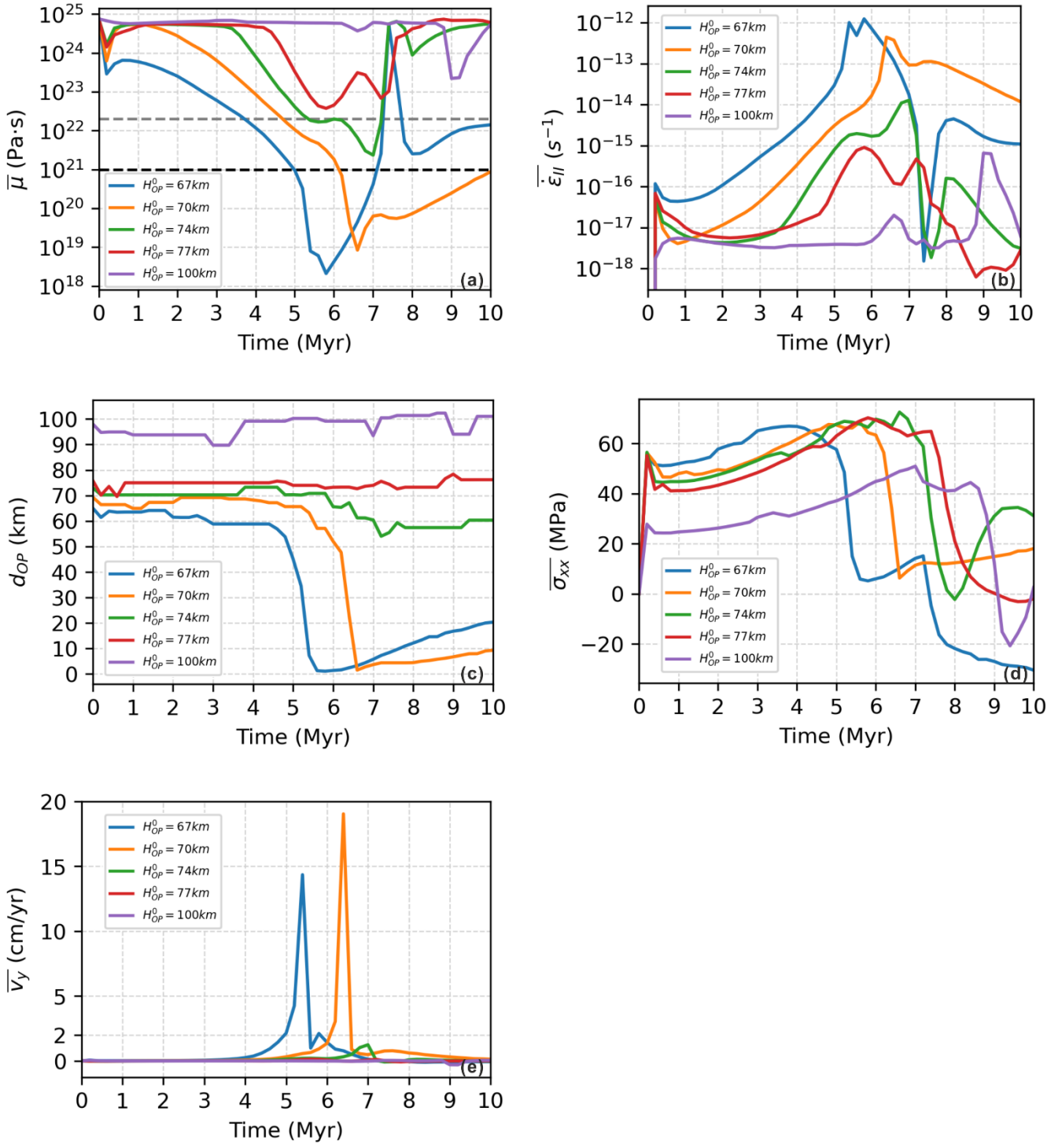
$$\bar{D} = \frac{1}{H_{OP}} \int_0^{H_{OP}} D \ dy, \quad (13)$$

340 in which D represent the diagnostic. The averaged results include magnitude of viscosity ($\bar{\mu}$),
 341 second invariant of strain rate ($\bar{\varepsilon}_{II}$), lithosphere thickness (\bar{d}_{OP}), horizontal stretching stress
 342 component ($\bar{\sigma}_{xx}$) and vertical velocity component (\bar{v}_y).

343 Take the model ' $H_{OP}^0 = 67$ km' for example (blue line, Figure 7), there is gradual increase of $\bar{\varepsilon}_{II}$ and
 344 $\bar{\sigma}_{xx}$, and gradual decrease of $\bar{\mu}$ during the simulation between 1 Myr to 4 Myr. While \bar{d}_{OP} and \bar{v}_y
 345 remains nearly constant. From 4 Myr to 5 Myr, $\bar{\varepsilon}_{II}$ and $\bar{\mu}$ keep a similar slope trend as before.
 346 While $\bar{\sigma}_{xx}$ stops increasing and starts to decrease gently. \bar{v}_y starts to increase and \bar{d}_{OP} starts to
 347 decrease. During the rifting and spreading extension between 5 Myr to 6 Myr, all diagnostics are
 348 varying more rapidly, with $\bar{\mu}$, \bar{d}_{OP} and $\bar{\sigma}_{xx}$ dropping and $\bar{\varepsilon}_{II}$, \bar{v}_y climbing steeply. The jump in \bar{v}_y
 349 couples with passive upwelling mantle flow as rifting extension initiates. Afterwards, the weakening
 350 process is replaced by a strengthening process where $\bar{\mu}$ and \bar{d}_{OP} both increase while $\bar{\varepsilon}_{II}$ and \bar{v}_y
 351 decrease gradually.

352 As the thickness of the overriding plate increases from 67 km to 100 km, the magnitude of viscosity
 353 drop in the necking area decreases. In detail, the plotting (Figure 7, a, grey dashed line) shows that

354 if $\bar{\mu}$ in the necking area of the overriding plate is above $\sim 2 \times 10^{22} \text{ Pa} \cdot \text{s}$, there is no lithospheric
355 thinning in the necking region (Figure 7, c, purple and red lines). In the timesteps when $\bar{\mu}$ is in the
356 range of $10^{21} - 2 \times 10^{22} \text{ Pa} \cdot \text{s}$, thinning starts to build up, but it is not weak enough to have rifting
357 extension (Figure 7, c, green line). Only when the $\bar{\mu}$ drops below $10^{21} \text{ Pa} \cdot \text{s}$ does significant
358 thinning develop within the overriding plate (Figure 7, c, blue and orange lines). The results of $\bar{\mu}$
359 confirms that the iso-viscous contour $10^{21} \text{ Pa} \cdot \text{s}$ can be used to predict if rifting or spreading
360 extension develops during the dual inward dipping subduction. It also reveals a more precise
361 maximum viscosity below which the thinning of lithosphere develops.



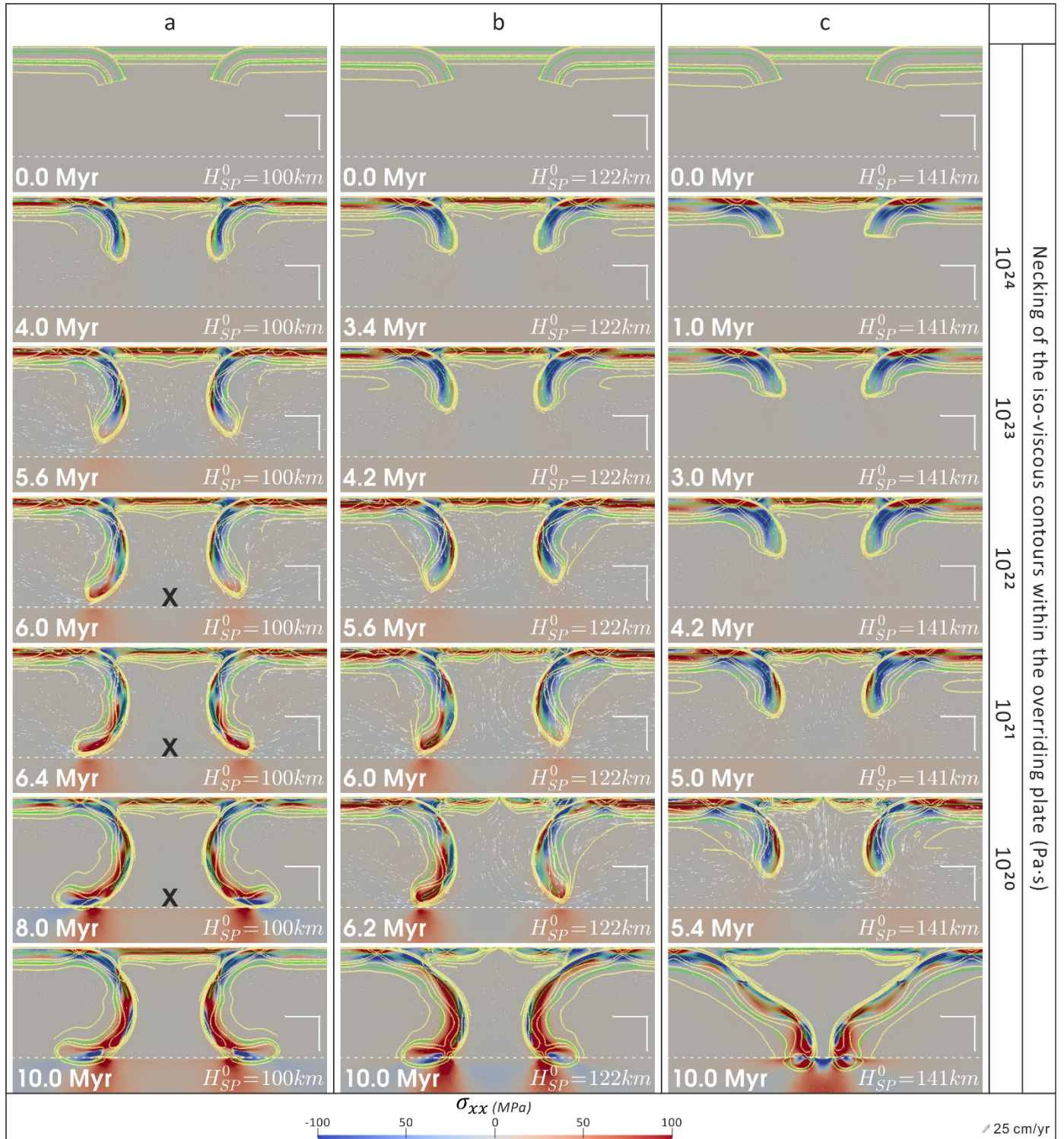
362

363 Figure 7. Temporal evolution of averaged diagnostics along the vertical slice in the middle of the overriding plate, (a) viscosity ($\bar{\mu}$),
364 (b) second invariant of strain rate ($\bar{\epsilon}_{II}$), (c) lithosphere thickness (\bar{d}_{OP}), (d) horizontal stretching stress component ($\bar{\sigma}_{xx}$) and (e)
365 vertical velocity component (\bar{v}_y). Positive value of \bar{v}_y represent upward motion.

366 3.4 Thickness of the subducting plate

367 The third series of models investigate increasing the initial thermal thickness (again as defined by

368 the 1300 K contour) of the subducting plate (H_{SP}^0) from 94 km to 141 km (Figure 8), while keeping
369 the overriding plate's thickness (H_{OP}^0) and the length of the overriding plate (L_{OP}^0) constant. As H_{SP}^0
370 increases, the maximum weakening level developed within the overriding plate increases from 'I'
371 ($H_{SP}^0 = 94 \text{ km}$) to 'III' ($H_{SP}^0 = 122 \text{ km}$) and 'IV' ($H_{SP}^0 = 141 \text{ km}$). The time it takes to lower each order
372 of viscosity magnitude decreases, indicating a faster progressive weakening.

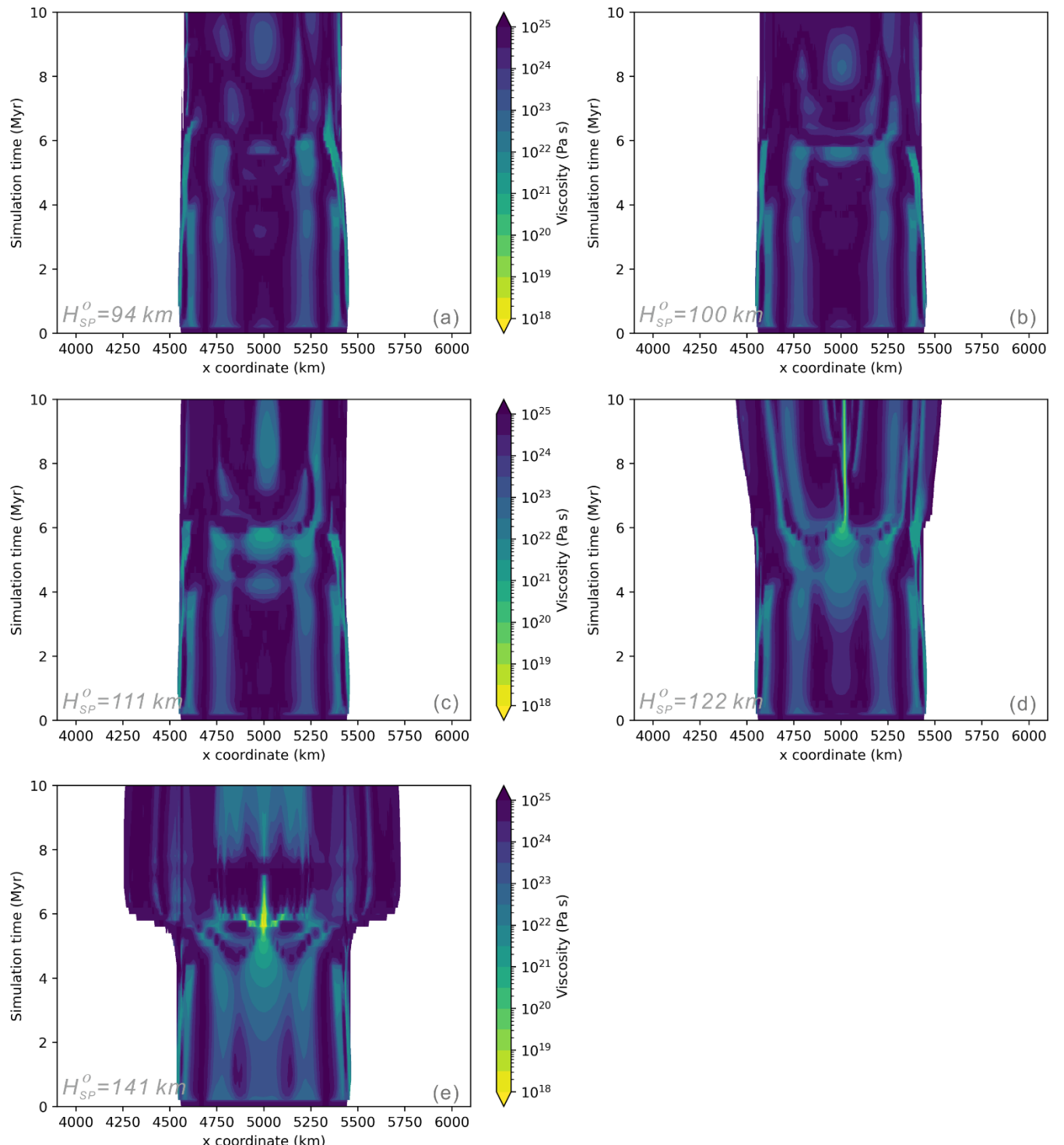


373
 374 Figure 8. Progressive weakening of the overriding plate during dual inward dipping subduction with increasing age of the subducting
 375 plate. (a) Model ' $H_{SP}^0 = 100 \text{ km}$ '. (b) Model ' $H_{SP}^0 = 122 \text{ km}$ '. (c) Model ' $H_{SP}^0 = 141 \text{ km}$ '. A detailed explanation of the contours and
 376 symbols could be found in the caption of Figure 2.

377 Besides, the total extension increases from $\sim 0 \text{ km}$ ($H_{SP}^0 \leq 111 \text{ km}$, Figure 9, a-c) to $\sim 200 \text{ km}$ ($H_{SP}^0 =$
 378 122 km , Figure 9, d) and ultimately to $\sim 600 \text{ km}$ ($H_{SP}^0 = 141 \text{ km}$, Figure 9, e). The maximum viscosity
 379 reduction in both the primary and secondary necking regions increases as H_{SP}^0 increases, while

380 the lateral distance away from the trench of necking regions are equal, showing little correlation

381 with H_{SP}^0 .



382

383 Figure 9. Temporal evolution of viscosity along a horizontal line at the depth of 5km in the overriding plate. (a) Model ' $H_{SP}^0 = 94 \text{ km}$ '.
384 (b) Model ' $H_{SP}^0 = 100 \text{ km}$ '. (c) Model ' $H_{SP}^0 = 111 \text{ km}$ '. (d) Model ' $H_{SP}^0 = 122 \text{ km}$ '. (e) Model ' $H_{SP}^0 = 141 \text{ km}$ '. Both models have the
385 same H_{OP}^0 (67 km) and L_{OP}^0 (500 km). The edge of the contour filling in the lateral direction represents the interface between the
386 overriding plate and subducting plate.

387 **3.5 Regime of stretching state**

388 A variety of deformation patterns and stretching state within the overriding plate have been
 389 observed when varying L_{OP}^0 , H_{SP}^0 and H_{OP}^0 . Several diagnostics are reported together to quantify
 390 the deformation developed within the overriding plate during the 10 Myr simulation (Table 3). The
 391 detail of each diagnostic is described as follows.

392 Table 3. Summary of diagnostics for all models. For further description of the diagnostics please see the main text.

| Model name | weakeni ng level | t_{rift} (Myr) | t_{660} (Myr) | l_{n2n} (km) | total strain |
|------------------------------|---------------------|----------------------------|--------------------|-------------------|------------------|
| $H_{SP}^0 = 94 \text{ km}$ | I | - | 6.6 | 0 | 1% |
| $H_{SP}^0 = 100 \text{ km}$ | III | - | 6.4 | 0 | 2% |
| $H_{SP}^0 = 111 \text{ km}$ | III | - | 6.4 | 0 | 21% |
| $H_{SP}^0 = 122 \text{ km}$ | IV | 6.2 | 6.4 | 0 | 110% |
| $H_{SP}^0 = 141 \text{ km}$ | IV | 5.4 | 6.0 | 0 | 2800% |
| $H_{OP}^0 = 67 \text{ km}$ | IV | 5.4 | 6.0 | 0 | 2800% |
| $H_{OP}^0 = 70 \text{ km}$ | IV | 6.4 | 6.6 | 0 | 1300% |
| $H_{OP}^0 = 74 \text{ km}$ | III | - | 7.2 | 0 | 30% |
| $H_{OP}^0 = 77 \text{ km}$ | II | - | 7.6 | 0 | 4% |
| $H_{OP}^0 = 100 \text{ km}$ | I | - | 8.8 | 0 | 1% |
| $L_{OP}^0 = 500 \text{ km}$ | IV | 5.4 | 6.0 | 0 | 2800% |
| $L_{OP}^0 = 600 \text{ km}$ | IV | 5.4 | 6.0 | 0 | 690% |
| $L_{OP}^0 = 700 \text{ km}$ | IV | 5.6 | 6.0 | 130 | 630% |
| $L_{OP}^0 = 800 \text{ km}$ | IV | 5.8 | 6.0 | 231 | 14% ^a |
| $L_{OP}^0 = 1000 \text{ km}$ | III | - | 6.0 | 282 | 15% |
| $L_{OP}^0 = 1200 \text{ km}$ | III | - | 5.8 | 621 | 11% |
| $L_{OP}^0 = 1600 \text{ km}$ | II | - | 5.4 | 937 | 4% |

393 ^a The total strain listed here is calculated along the middle vertical slice (5000 km away from side boundaries). For models $L_{OP}^0 \geq$
 394 800 km, the necking zones are away from this middle vertical slice. So, the total strain could be underestimated for these models.
 395 Considering that only model ' $L_{OP}^0 = 800 \text{ km}$ ' achieved weakening level 'IV', the corrected total strain along its necking zone is $\sim 600\%$.
 396 While the underestimation for other models is moderate and will not change the conclusion of this research.

397 As introduced in section 3.1.1, weakening levels 'I', 'II', 'III', 'IV' are determined by the minimum
 398 viscosity contour which is necked in the overriding plate during subduction. The higher the
 399 weakening level, the stronger the localised rheology modification observed within the overriding
 400 plate. All three groups of dual inward dipping subduction models manage to yield a variety of

401 weakening levels in the overriding plate (Figure 10, a-c).

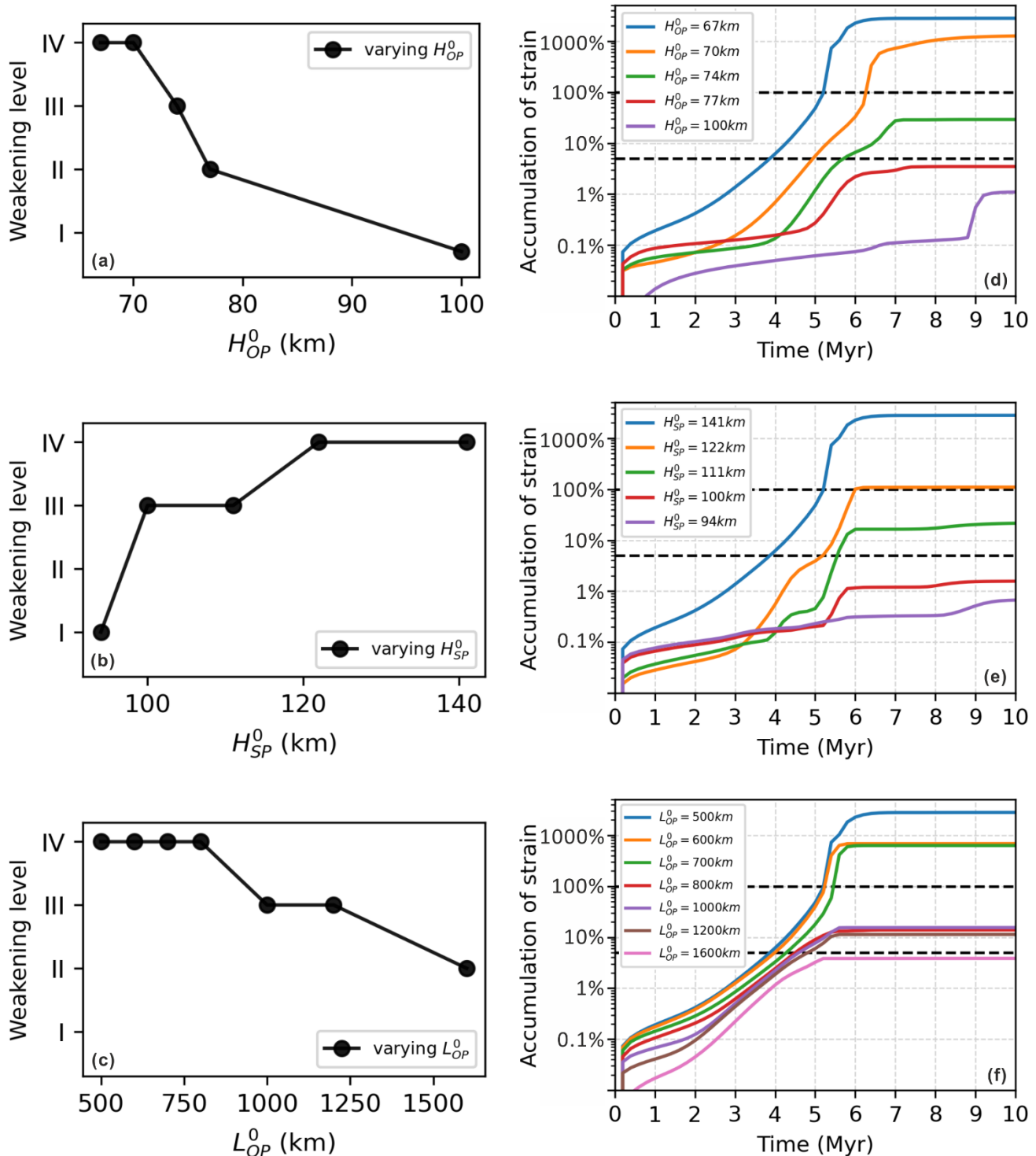
402 t_{rift} indicates the timestep when the overriding plate develops rifting extension (weakening level
403 ‘IV’), and a void value means that model fails to generate rifting extension within the overriding
404 plate. It shows that only models achieving weakening level ‘IV’ develop rifting extension. t_{rift}
405 increases with thicker or longer overriding plate, and decreases with thicker subducting plate.

406 t_{660} equals how much time the subducting plate (defined by its 1300 K isotherm) takes to sink to
407 the depth of 660km. It is most sensitive to the variation of H_{OP}^0 , while varying L_{OP}^0 and H_{SP}^0
408 generates less than ~1 Myr difference of t_{660} compared with a ~3 Myr difference when modifying
409 H_{OP}^0 .

410 l_{n2n} is the horizontal distance between necking centres which may develop rifting extension during
411 dual inward dipping subduction, i.e., secondary necking regions are excluded. The value of l_{n2n} is
412 0 km if there is only one necking centre within the overriding plate. l_{n2n} starts to increase with L_{OP}^0
413 when L_{OP}^0 is greater than ~700 km. l_{n2n} in Table 3 is recorded at the timestep of 4.4 Myr, which
414 was selected to be before significant transition that occurs when the slab interacts with the lower
415 mantle. It should be noted that, l_{n2n} may vary with time and the difference is at most ~250 km
416 (Figure 4).

417 Total strain is calculated by integrating the average strain rate ($\overline{\dot{\epsilon}_{II}}$ based on Equation (13)) with
418 time throughout the 10 Myr simulation. All three groups of models generate a variety of total strain
419 at the end of the simulation (Figure 10, d-f). For all models that develop rifting extension, the total
420 strain is greater than 100%. Total strain in the range of 5% to 100% is observed from limited thinning

421 up to significant extension. For models where the total strain is less than 5%, the weakening
 422 deformation is hardly observable in the overriding plate.



423
 424 Figure 10. Key diagnostics used to characterise the rheology modification within the overriding plate. (a-c) Weakening level
 425 developed within the overriding plate. (d-f) Accumulation of strain in the middle of the overriding plate (5000 km away from the side
 426 boundaries).

427 By combining all the qualitative and quantitative diagnostics presented in these results, we classify
428 three stretching states: 1) little or no lithosphere thinning and extension, discriminated by low
429 weakening level up to level ‘II’, little total strain up to 5% and almost no thermal lithosphere thinning
430 in the necking area; 2) limited lithosphere thinning and extension, identified by medium weakening
431 level up to level ‘III’, medium total strain up to 30%, and limited thermal lithosphere thinning, e.g.,
432 ~15 km thinning for model ‘ $H_{OP}^0 = 74 \text{ km}$ ’ (Figure 7, c); 3) rifting and spreading extension,
433 characterised by high weakening level up to level ‘IV’, high total strain over 100%, and total thinning
434 of the thermal lithosphere during rifting extension.

435 4. Discussion

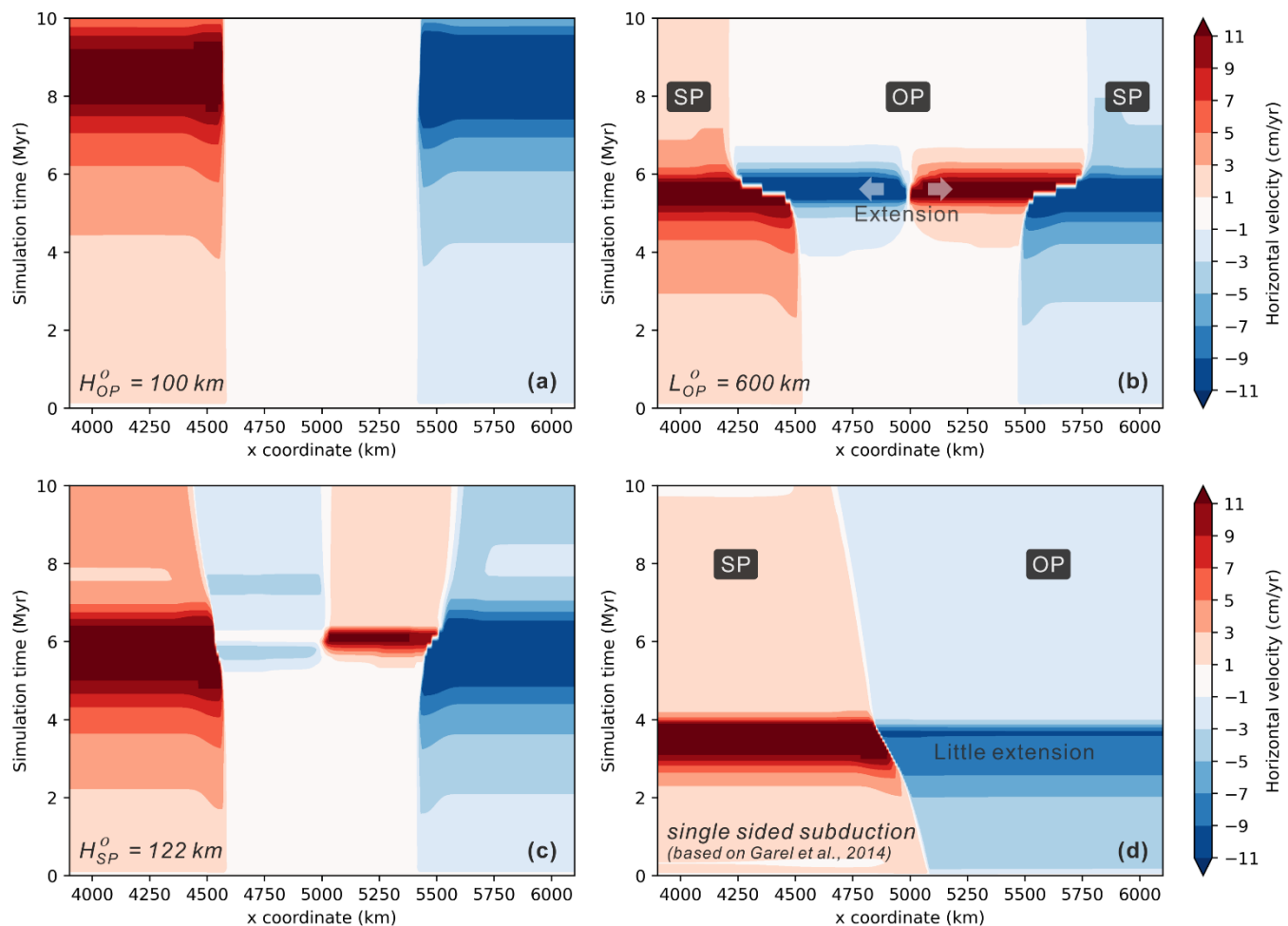
436 The results show that dual inward dipping subduction can induce progressive weakening within a
437 uniform overriding plate. With appropriate conditions, tested in this research, e.g., thick enough
438 H_{SP}^0 , thin enough H_{OP}^0 , short enough L_{OP}^0 , different levels of stretching state, ranging from no
439 thinning nor extension to rifting and spreading extension, can develop within the homogeneous
440 overriding plate. The role that dual inward dipping subduction plays during the progressive
441 weakening and the origin of the softening process are worth discussion.

442 4.1 The role dual inward dipping subduction plays

443 4.1.1 *Creating fixed trailing boundary condition for the overriding plate*

444 Due to the symmetric model setup, subducting plates on both sides are prone to (at least initially)
445 advance or retreat simultaneously. This creates roughly equal, symmetric and competing force from

446 both ends of the overriding plate during subduction. As a result, the mobility of the overriding plate
 447 is inhibited, as indicated by the low velocity (<1 cm/yr, white contour) region within the overriding
 448 plate (Figure 11, a-c). It would be as if the mechanical boundary condition on the overriding plate
 449 was fixed. As the overriding plate keeps weakening during dual inward dipping subduction,
 450 divergent velocity difference can build up within the overriding plate, indicating initiation of extension
 451 (Figure 11, b-c).



452
 453 Figure 11. Temporal evolution of horizontal velocity component along a lateral slice, x coordinate from 3900km to 6100 km, at the
 454 depth of 20 km from the surface. (a) model ' $H_{OP}^0 = 100 \text{ km}$ ', (b) model ' $L_{OP}^0 = 600 \text{ km}$ ', (c) model ' $H_{SP}^0 = 122 \text{ km}$ ', (d) single sided
 455 subduction with a mobile overriding plate referring to (b) model ' $L_{OP}^0 = 600 \text{ km}$ '. The contour filling represents the variation of
 456 horizontal component of velocity vector throughout the 10 Myr simulation. Positive value means right-ward motion and negative
 457 value is left-ward motion. The white area represents that the plate is nearly stagnant. And the edge of the white area marks the
 458 interface between the subducting plate and overriding plate or rifting and spreading centre within the overriding plate. SP and OP
 459 are short for subducting plate and overriding plate separately.

460 Previous studies on single-sided subduction cases have implied that the mobility of the overriding
461 plate plays an important role in producing extension, especially in the back-arc region of the
462 overriding plate. A mobile overriding plate can move as a whole to inhibit the build-up of deviatoric
463 stress within the plate (Capitanio et al., 2010; Chen et al., 2016; Garel et al., 2014; Holt et al., 2015;
464 Nakakuki and Mura, 2013), while the immobile overriding plate can facilitate strain localisation
465 which accounts for the increased degree of deformation in the overriding plate compared with
466 mobile plates (Capitanio et al., 2010; Chen et al., 2016; Erdős et al., 2021; Nakakuki and Mura,
467 2013; Yang et al., 2019).

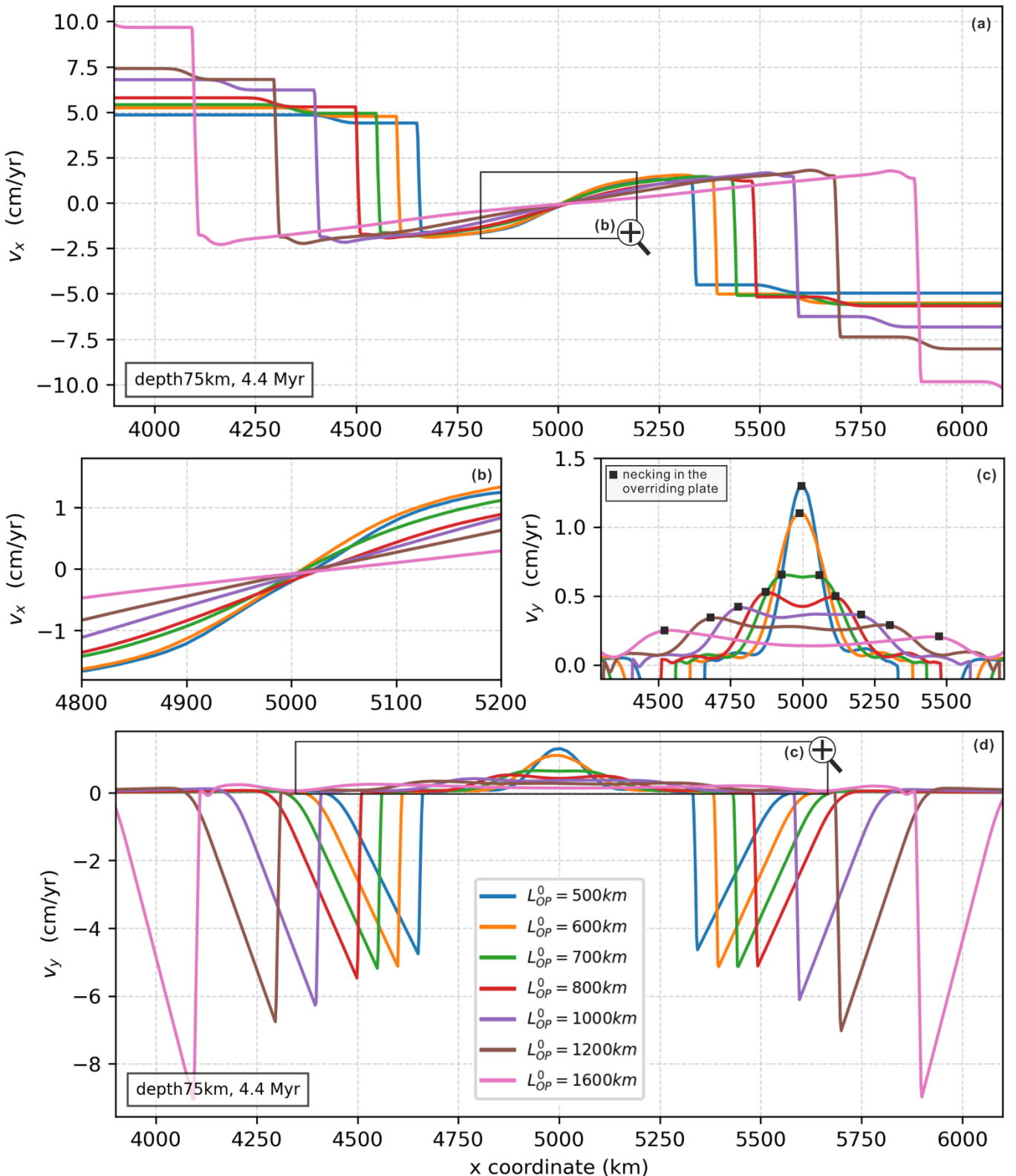
468 To investigate the role of fixed trailing boundary condition in promoting extension, we consider a
469 single sided subduction (SSS) model with a free and mobile overriding plate, based on previous
470 SSS research (Garel et al., 2014). The SSS model has the same parameters as the dual inward
471 dipping subduction model ' $L_{OP}^0 = 600 \text{ km}$ ' in every aspect, e.g., rheology, initial subduction plate
472 thickness (141 km) and initial overriding plate thickness (67 km) at the trench, except that there is
473 only one subducting plate and the overriding plate holds a mobile side boundary. The results show
474 that much less extension, evidenced by the magnitude of divergent velocity difference, is observed
475 in the overriding plate of SSS model (Figure 11, d) relative to that in the model ' $L_{OP}^0 = 600 \text{ km}$ '
476 (Figure 11, b). Thus, the lack of mobility of the overriding plate plays a key role in promoting the
477 degree of weakening during dual inward dipping subduction.

478 **4.1.2 Stronger poloidal return flow**

479 Our results show that varying the size of the overriding plate can affect the degree of extension
480 within the overriding plate. Previous research shows that subduction can induce poloidal mantle

481 return flow, which has been suggested to account for extensional deformation within the overriding
482 plate, e.g., back-arc extension, supercontinent breakup (Chen et al., 2016; Dal Zilio et al., 2018;
483 Erdős et al., 2021; Gerardi and Ribe, 2018; Sleep and Toksöz, 1971). Previous research also
484 implies that, a) increasing the thickness of the subducting plate (H_{SP}^0) can increase the net negative
485 buoyancy thus leading to a stronger poloidal flow (Garel et al., 2014); b) lowering the thickness of
486 the overriding plate (H_{OP}^0) can not only increase the net negative buoyancy by increasing the
487 hanging slab area in the upper mantle, but also reduces the dissipation during subduction along
488 the interface between two plates (Erdős et al., 2021). These two mechanisms also come into play
489 for dual inward dipping subduction models.

490 In addition, dual inward dipping subduction models can yield a third way to strengthen the return
491 flow. This is by combining the two separate poloidal convection flows, one from each subducting
492 plate, as the length of the overriding plate (L_{OP}^0) shortens (Figure 3). This is shown for example by
493 the velocity variation in both the horizontal (v_x) and vertical (v_y) direction at the depth of 75 km
494 (Figure 12). For all dual inward dipping subduction models, the magnitude of v_x decreases
495 gradually from ~2.5 cm/yr in the mantle wedge corner to 0 cm/yr underlying the middle part (~5000
496 km away from side boundaries) of the overriding plate (Figure 12, a). As L_{OP}^0 changes, models with
497 shorter overriding plate have greater v_x gradient along the lateral slice (Figure 12, b). The
498 maximum magnitude of v_y increases from ~0.25 cm/yr to ~1.3 cm/yr, implying a faster upwelling
499 flow, as the length of the overriding plate (L_{OP}^0) shortens (Figure 12, c-d). It is also noted that the
500 necking area developed within the overriding plate (e.g., Figure 3) lies right above the maximum
501 upwelling component of the return flow (Figure 12, c), suggesting a spatial correlation between the
502 stronger poloidal return flow and the progressive weakening in the overriding plate.



503
504
505
506
507
508
509

Figure 12. Velocity variation along a slice at the depth of 75 km, which is ~8 km below the 1300 K isotherm of the overriding plate, after 4.4 Myr simulation. (a, d) Horizontal and vertical component of velocity along the slice. (b) and (c) are zoom-in of (a) and (d) under the middle part of the overriding plate (5000 ± 200 km and 5000 ± 650 km away from the side boundaries respectively). Positive value means rightward or upward motion, and negative value represents leftward or downward motion. In (c), the horizontal coordinate of the necked region in the overriding plate is plotted as black square to visualize its spatial correlation with upwelling component of mantle wedge flow. All plots share the same legend listed in (d).

510 Previous research on subduction shows that the return flow can apply basal traction, which can
511 propagate upwards and create high enough extensional stress that overcome the strength of the
512 overriding plate (e.g., Capitanio et al., 2010; Holt et al., 2015). A united, thus stronger return flow is
513 likely to strengthen the mantle flow's ability to weaken the overriding plate, as indicated in Figure 3
514 and Figure 12. Meanwhile, the extension during progressive weakening can also drive passive
515 upwelling mantle flow, which can reinforce the spatial correlation between the necking region and
516 the maximum magnitude of ν_y (Figure 12, c).

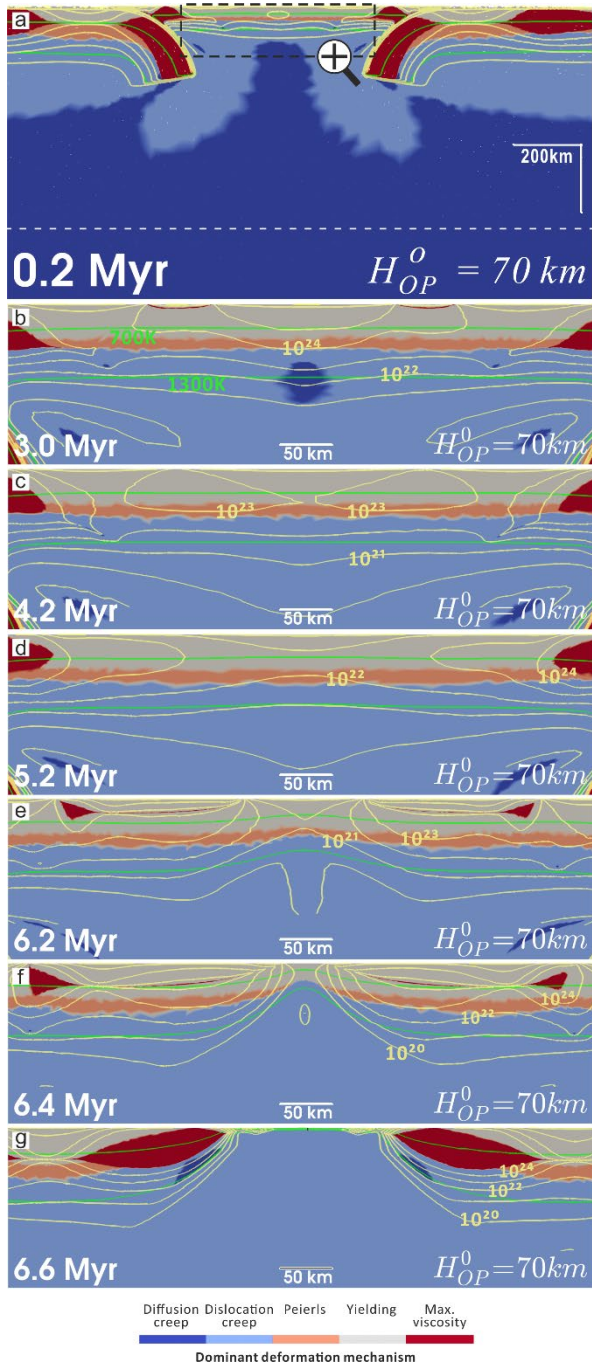
517 **4.2 Overriding plate weakening mechanism**

518 As introduced in the methods, we applied composite rheology which incorporates four deformation
519 mechanisms everywhere in the simulation domain. Here, the dominant deformation mechanism
520 (DDM) is defined as the rheology law that yields the minimum magnitude of viscosity at a certain
521 point. We try to understand the temporal and spatial evolution of the DDM within the overriding
522 plate, especially in the region where strain localisation takes place. Then we evaluate the
523 contribution of each deformation mechanism in promoting strain localisation within the overriding
524 plate.

525 **4.2.1 Dominant deformation mechanism analysis**

526 The reference model ' $L_{OP}^0 = 1200 \text{ km}$ ' with limited extension has shown that the DDM is stratified
527 with yielding, Peierls creep and dislocation creep as the depth increases within the overriding plate
528 (Figure 2, b). Here, we further investigate how the DDM evolves in models that develop rifting and
529 spreading extension within the overriding plate, e.g., model ' $H_{OP}^0 = 70 \text{ km}$ '. Therein, the temporal

530 phases show that the DDM is also spatially layered (Figure 13), with yielding initially dominating
531 from the surface to the depth of ~35 km, underlain by Peierls creep dominating for the next ~10 km
532 and then dislocation creep dominating for ~25 km (Figure 13, b-d). Among all the DDM at different
533 depths throughout the simulation, yielding is always the thickest and dislocation creep comes as
534 the second. To be noted, the DDM of diffusion creep with limited area is observed around the bottom
535 of the overriding plate during the initial plate weakening (Figure 13, b), and it is completely replaced
536 by dislocation creep after 3.6 Myr. During the thinning process of the overriding plate, the
537 deformation mechanism of Peierls creep gives way to yielding and dislocation creep as DDM
538 (Figure 13, d-g). The replacement and interplay among different DDM will be discussed in the next
539 subsection.



540

541 Figure 13. Temporal evolution of the dominant deformation mechanism within the overriding plate in model $H_{OP}^0 = 70 \text{ km}$. The
542 dashed zoom-in block in (a) shows the location of screenshots in (b-g). The progressive weakening process within the overriding
543 plate is demonstrated by the necking of the iso-viscous contours. The 5 groups of yellow contours encompassing the plates in each
544 screenshot are iso-viscous contours of $10^{20}, 10^{21}, 10^{22}, 10^{23}, 10^{24} \text{ Pa} \cdot \text{s}$ from outward to inward. The two sets of green solid lines
545 are 700 K and 1300 K isotherm contours to image the geometry of the thermal plate. The bottom left corner caption shows the
546 elapsed simulation time and bottom right corner is the name of the model.

547

While we do not implement a multi-material approach to define the rheology of different layers in
the lithosphere, the uniform compositional rheology law self-consistently generates the layered
structure in Figure 13. In detail, yielding only dominates over other creep mechanisms in the cold

548

549

550 regions, corresponding to the crustal depth range. While dislocation and diffusion creep dominate
551 over yielding in the hot bottom region, equivalent to the depth range of mantle lithosphere. The
552 continuous necking process shows that the viscosity reduction initiates from the surface (yielding)
553 and the bottom of the plate (dislocation creep). Then the viscosity contour necks in the middle depth
554 of the plate as seen in Figure 13, (b-e). This suggests that yielding and dislocation creep play the
555 dominant role in promoting the continuous weakening of the overriding plate.

556 **4.2.2 Weakening contribution analysis**

557 The previous section has shown that the DDM may vary at different depth range within the
558 overriding plate. To evaluate the contribution of each DDM to inducing rifting and spreading
559 extension for each timestep, we slice the overriding plate vertically through its middle where the
560 most intensive necking takes place. Then we group the points along the midline by the type of DDM.
561 Two kinds of calculation are conducted. 1) For the points with the same DDM, we calculate at each
562 timestep the arithmetic average of the strain rate and temperature state which can be used to
563 compute the viscosity through Equation (8). 2) We compute the minimum viscosity among all points
564 along the midline, and define the DDM that yields the minimum viscosity as the Minimum Viscosity
565 Dominant Deformation Mechanism (MVDDM). To be clear, the DDM is calculated at each point
566 independent of other points, while the MVDDM is calculated using all relevant points along the
567 midline.

568 One diagnostic to evaluate the contribution of deformation mechanisms to plate weakening is to
569 quantify how much (order of) viscosity reduction each DDM achieves. For model ' $H_{OP}^0 = 70 \text{ km}$ ',
570 both yielding and dislocation creep reduces the viscosity to lower than $10^{21} \text{ Pa} \cdot \text{s}$ (Figure 14, a),

571 which is the critical magnitude to initiate rifting and spreading extension (Figure 7, a). While Peierls
572 creep can reduce viscosity to the range of 10^{21} - $10^{22} \text{ Pa} \cdot \text{s}$, which can enable limited thinning but
573 it fails to induce rifting extension. Diffusion creep induces the least viscosity reduction to
574 $\sim 5 \times 10^{22} \text{ Pa} \cdot \text{s}$, which suggests that it only softens the plate for further deformation through limited
575 viscosity reduction. For models that do not develop rifting or spreading extension, the temporal
576 paths of the DDM are similar with model ' $H_{OP}^0 = 70 \text{ km}$ ' except that the minimum viscosity is never
577 less than $10^{21} \text{ Pa} \cdot \text{s}$. Another diagnostic to evaluate the contribution of deformation mechanisms
578 to plate weakening is how long it stays active. We note that yielding and dislocation creep are two
579 types of DDM that are active throughout the simulation (Figure 14, a), while diffusion creep and
580 Peierls creep disappears as DDM along the midline after 3.6 Myr and 6.4 Myr separately (Figure
581 13, b, f).

582

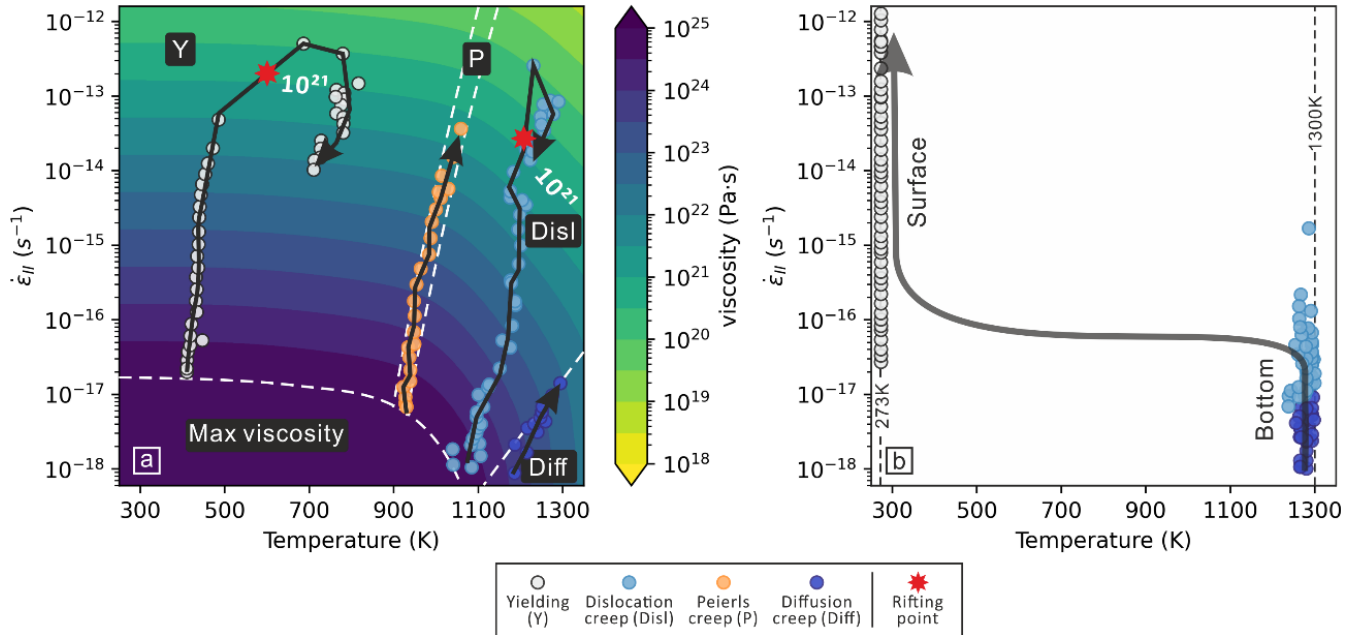


Figure 14. Scatter plots of the dominant deformation mechanism along the midline of the overriding plate (5000 km away from both side boundaries), i.e., the main necking region. (a) The temporal path of each dominant deformation mechanism (DDM) is plotted on a phase diagram, where the magnitude of viscosity is calculated based on Equation (7). The phase diagram is divided by the white dashed lines into four domains based on the calculation of which component deformation mechanism yields the minimum viscosity at the given strain rate, temperature and depth. The fifth domain marks the maximum viscosity. To be noted, the depth used to create the viscosity contour is 50 km, which may not reflect the complete temporal path but it helps to demonstrate how viscosity will evolve. The scatter points are taken from the model ' $H_{OP}^0 = 70 \text{ km}$ ', and each point is calculated by averaging the strain rate and temperature state at each timestep for the portion of the midline that holds the same dominant deformation mechanism. (b) The evolution of the dominant deformation mechanism that yields the minimum viscosity (MVDDM) throughout the midline of the overriding plate. Scatter points are taken from 5 models with varying thickness of the overriding plate (H_{OP}^0).

To be noted, we observe an accelerating viscosity reduction in the range of $10^{20}\text{-}10^{22} \text{ Pa} \cdot \text{s}$ for the DDM of yielding and dislocation creep (Figure 14, a). That is when plate thinning, rifting and spreading extension take place. The accelerating viscosity reduction suggests that the overriding plate falls into positive feedback weakening loops as strain localises in the necking region. Such self-strengthening weakening feedback loop when necking develops into a rifting centre is also reported in previous research using power-law viscous creeping flow law with an exponent > 1 (Wenker and Beaumont, 2018). As in the case of uniaxial stretching, the plate strength is proportional to $\bar{\mu} \times H_{OP}$ (Ribe, 2001), both of which in our models are reducing during the plate thinning process. Since the plate strength measures the very resistance to the underlying mantle

603 flow, the reduction of viscosity and plate thickness will incur further plate weakening. The
604 continuous plate strength reduction during dual inward dipping subduction may end up with the
605 formation of new plate boundaries.

606 The location of the weakest point (with the least viscosity) along the midline migrates from the
607 bottom of the overriding plate to the surface as dual inward dipping subduction proceeds (Figure
608 14, b). Correspondingly, the MVDDM changed from diffusion creep and dislocation creep at the
609 bottom of the plate to yielding at the surface. Such a transition is observed no matter whether only
610 rifting or full spreading extension develops within the overriding plate. The result indicates that the
611 transition is enabled as long as the strain rate can keep increasing during subduction (Figure 14,
612 b). Though, only a high enough strain rate ($\sim 10^{-13} \text{ s}^{-1}$) can lower the viscosity ($\sim 10^{21} \text{ Pa} \cdot \text{s}$)
613 sufficiently through yielding and dislocation creep to induce rifting and spreading extension (Figure
614 14, a).

615 While the rheology law (Equation (8-9)) of the four deformation mechanisms shows that the
616 magnitude of viscosity is dependent on evolving temperature, strain rate, and lithostatic pressure,
617 the diagram (Figure 14, a) indicates that the viscosity reduction is mainly driven by the ever-
618 increasing strain rate relative to the much gentler impact of increasing thermal gradient and
619 decreasing lithostatic pressure due to plate thinning. The dominant role of strain rate-induced
620 weakening over thermal weakening is also reported in the interaction between upwelling plumes
621 and overlying lithosphere (Burov and Guillou-Frottier, 2005). That is to say, the rheology and
622 buoyancy parameters will be more important than the heat conduction parameters in producing
623 different levels of rheology weakening within the overlying plate. The continuously growing strain

rate can also explain the replacement of diffusion creep by dislocation creep as the DDM at the bottom of the overriding plate. While the replacement of Peierls creep by yielding or dislocation creep as DDM during the plate thinning process is likely due to both increasing strain rate and temperature at the intermediate depth. In addition, the strain rate induced weakening is also a precondition to initiate thermal weakening, lithosphere thinning, strain localisation and formation of new plate boundaries (eg. Fuchs and Becker, 2021, 2019; Gueydan et al., 2014).

4.3 Limitations

The major contribution of this work is incorporating a composite rheology which depends on multiple parameters, e.g., temperature, strain rate etc., for the dual inward dipping subduction models, and investigating the driving mechanism of the progressive weakening in the overriding plate. However, previous research indicates that viscosity can also be affected by hydrous fluids, partial melting, and grain size of minerals in subduction zones (Bercovici et al., 2015; Braun et al., 1999; England and Katz, 2010; Montési and Hirth, 2003). In particular, grain size reduction is likely to take place when strain builds up and it may make diffusion creep become the dominant deformation mechanism, overtaking dislocation creep, in the mantle lithosphere (Gueydan et al., 2014; Ruh et al., 2022). Taking all these parameters into consideration is likely to strengthen the feedback weakening process within the overriding plate during dual inward dipping subduction, while at the cost of making the computation much more expensive (Foley, 2018).

Subduction can generate convective mantle flow that includes both poloidal and toroidal components. The 2D models tested here neglect the effects of toroidal flow and the third dimension. This could amplify the magnitude of poloidal flow and its weakening effect applied within the

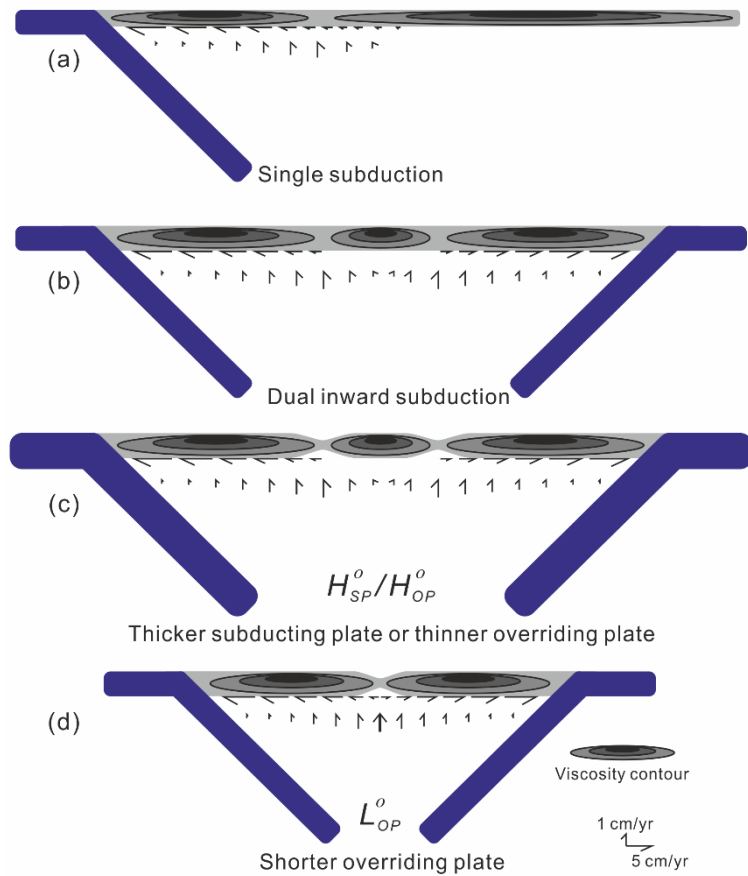
645 overriding plate. Considering that poloidal component dominates over toroidal component when
646 slab subducts through the upper mantle (Finciello et al., 2004), and it is the poloidal cell that
647 provides the relevant traction driving the deformation within the overriding plate (Király et al., 2017;
648 Schellart and Moresi, 2013), the lack of toroidal flow would only have limited impact on the
649 progressive weakening presented.

650 Bearing all the limits in mind, we cautiously compare our model predictions with observations in the
651 Caribbean Sea plate, which has experienced dual inward dipping subduction since at least ~60 Ma
652 (Boschman et al., 2014; Braszus et al., 2021), with the Farallon plate (subsequently, Cocos and
653 Nazca plates) subducting at the Central America Trench in the west and Proto-Caribbean plate
654 (followed by Atlantic plate) subducting at the Lesser Antilles Trench in the east. One interesting
655 observation from plate reconstruction is that the distance between the two trenches seems to have
656 increased since the establishment of the dual inward dipping subduction (Barrera-Lopez et al., 2022;
657 Boschman et al., 2014; Braszus et al., 2021; Romito and Mann, 2021), suggesting that the
658 Caribbean plate has undergone extension. The extension includes the formation of multiple basins
659 throughout the Caribbean Sea plate, e.g., Tobago Basin, Grenada Basin, Venezuela Basin and
660 Colombia Basin since ~60 Ma (Allen et al., 2019; Braszus et al., 2021; Romito and Mann, 2021).
661 The effect of the fixed boundary condition may play a role in promoting the extension, which may
662 originate from the development of the Caribbean Large Igneous Province (Pindell et al., 2006), and
663 multiple periods of back-arc extension as the Lesser Antilles Trench continuously retreats (Steel
664 and Davison, 2021). We note that there is uncertainty in plate reconstructions and limited evidence
665 on the timing of extension. Therefore, we must consider this comparison as somewhat speculative.
666 Further the two-dimensional nature of the models might not be a good representation of the

667 dynamics on the eastern side of the Caribbean plate with its narrow subduction zone.

668 **4.4 Synoptic summary**

669 The thermo-mechanical modelling here provides a generic understanding of the progressive
670 weakening developed within a varying viscosity overriding plate during dual inward dipping
671 subduction. To summarise, dual inward dipping subduction holds a stronger tendency to weaken
672 the overriding plate compared with single sided subduction. This is achieved by creating a fixed
673 trailing boundary condition for the overriding plate and generating a stronger poloidal return flow
674 underlying the overriding plate (Figure 15). The stronger poloidal mantle flow is exhibited as a
675 higher horizontal velocity gradient and higher maximum magnitude of upwelling component
676 underlying the overriding plate. It can also initiate a higher degree of viscosity reduction, strain
677 localisation and lithosphere thinning or even spreading extension within the overriding plate.
678 Besides, a dual inward dipping subduction system with thinner and shorter overriding plate, and
679 thicker subducting plate is likely to induce a higher degree of viscosity reduction within the
680 overriding plate (Figure 15, b-d).



681
682 Figure 15. Synoptic comparison of different model setup's role in affecting the necking behaviour developed within the overriding
683 plate. (a) Single sided subduction (Garel et al., 2014). (b) Dual inward dipping subduction. (c) Thickness of the subducting plate or
684 overriding plate (H_{SP}^0, H_{OP}^0). (d) Length of the overriding plate (L_{OP}^0).

685 5. Conclusion

686 These 2-D thermo-mechanical numerical models demonstrate that dual inward dipping subduction
687 can generate progressive weakening by lowering viscosity within the overriding plate on a ~10 Myr
688 time scale. Three variables are investigated to understand what controls the maximum degree of
689 weakening. It shows that the initial length (L_{OP}^0) and thickness (H_{OP}^0) of the overriding plate are
690 negatively correlated with the maximum degree of weakening. While the initial thickness of the
691 subducting plate (H_{SP}^0) positively relates to the maximum weakening level. The progressive
692 weakening can result in a variety of irreversible stretching states ranging from 1) little or no
693 lithosphere thinning and extension, to 2) limited thermal lithosphere thinning, and 3) localised rifting

694 followed by spreading extension.

695 Comparing with single-sided subduction, dual inward dipping subduction can reduce the magnitude
696 of viscosity to a lower level within the overriding plate. Two aspects are analysed. On the one hand,
697 a dual inward dipping subduction set-up effectively creates a dynamic fixed boundary condition for
698 the middle (overriding) plate. This inhibits the mobility of the plate and helps promote localised
699 strain to accommodate the slab rollback tendency on both sides. On the other hand, when the initial
700 length of the overriding plate is short enough ($L_{OP}^0 \leq 800 \text{ km}$), dual inward dipping subduction can
701 form a united upwelling mantle flow which interacts with the bottom of overriding plate and
702 generates a stronger viscosity perturbation within it than single sided subduction models. As a result,
703 dual inward dipping subduction can induce higher degrees of extension in the overriding plate
704 compared with single sided subduction.

705 During the progressive weakening, yielding and dislocation creep are the dominant deformation
706 mechanisms that initiates rifting and spreading extension. The progressive weakening is mainly
707 driven by the ever-increasing strain rate, which is also a precondition for initiating thermal
708 weakening, strain localisation, lithosphere thinning and formation of new plate boundaries.

709 **Acknowledgement**

710 We acknowledge the support of Advanced Research Computing at Cardiff (ARCCA) and the
711 Supercomputing Wales project, which is part-funded by the European Regional Development Fund
712 (ERDF) via the Welsh Government. Zhibin Lei also thanks the China Scholarship Council (CSC)
713 for supporting the Ph.D. studentship and Cardiff University for an overseas fee waiver award.

714 **References**

- 715 Allen, R.W., Collier, J.S., Stewart, A.G., Henstock, T., Goes, S., Rietbrock, A., Macpherson, C., Blundy, J., Davidson,
716 J., Harmon, N., Kendall, M., Prytulak, J., Rychert, C., Van Hunen, J., Wilkinson, J., Wilson, M., 2019. The role of
717 arc migration in the development of the Lesser Antilles: A new tectonic model for the Cenozoic evolution of the
718 eastern Caribbean. *Geology* 47, 891–895. <https://doi.org/10.1130/G46708.1>
- 719 Alsaif, M., Garel, F., Gueydan, F., Davies, D.R., 2020. Upper plate deformation and trench retreat modulated by
720 subduction-driven shallow asthenospheric flows. *Earth Planet. Sci. Lett.* 532, 116013.
721 <https://doi.org/10.1016/j.epsl.2019.116013>
- 722 Barrera-Lopez, C. V., Mooney, W.D., Kaban, M.K., 2022. Regional Geophysics of the Caribbean and Northern South
723 America: Implications for Tectonics, Geochemistry, Geophys. Geosystems 23, 1–24.
724 <https://doi.org/10.1029/2021GC010112>
- 725 Bercovici, D., Tackley, P.J., Ricard, Y., 2015. The Generation of Plate Tectonics from Mantle Dynamics, in: Treatise on
726 Geophysics: Second Edition. Elsevier B.V., Oxford, pp. 271–318. <https://doi.org/10.1016/B978-0-444-53802-4.00135-4>
- 728 Boschman, L.M., van Hinsbergen, D.J.J., Torsvik, T.H., Spakman, W., Pindell, J.L., 2014. Kinematic reconstruction of
729 the caribbean region since the early jurassic. *Earth-Science Rev.* 138, 102–136.
730 <https://doi.org/10.1016/j.earscirev.2014.08.007>
- 731 Braszus, B., Goes, S., Allen, R., Rietbrock, A., Collier, J., Harmon, N., Henstock, T., Hicks, S., Rychert, C.A., Maunder,

- 732 B., van Hunen, J., Bie, L., Blundy, J., Cooper, G., Davy, R., Kendall, J.M., Macpherson, C., Wilkinson, J., Wilson,
733 M., 2021. Subduction history of the Caribbean from upper-mantle seismic imaging and plate reconstruction. Nat.
734 Commun. 12. <https://doi.org/10.1038/s41467-021-24413-0>
- 735 Braun, J., Chéry, J., Poliakov, A., Mainprice, D., Vauchez, A., Tomassi, A., Daignières, M., 1999. A simple
736 parameterization of strain localization in the ductile regime due to grain size reduction: A case study for olivine. J.
737 Geophys. Res. Solid Earth 104, 25167–25181.
- 738 Bürgmann, R., Dresen, G., 2008. Rheology of the lower crust and upper mantle: Evidence from rock mechanics,
739 geodesy, and field observations. Annu. Rev. Earth Planet. Sci. 36, 531–567.
740 <https://doi.org/10.1146/annurev.earth.36.031207.124326>
- 741 Burov, E., Guillou-Frottier, L., 2005. The plume head-continental lithosphere interaction using a tectonically realistic
742 formulation for the lithosphere. Geophys. J. Int. 161, 469–490. <https://doi.org/10.1111/j.1365-246X.2005.02588.x>
- 743 Burov, E.B., 2011. Rheology and strength of the lithosphere. Mar. Pet. Geol. 28, 1402–1443.
744 <https://doi.org/10.1016/j.marpetgeo.2011.05.008>
- 745 Byerlee, J., 1978. Friction of rocks. Pure Appl. Geophys. PAGEOPH 116, 615–626.
746 <https://doi.org/10.1007/BF00876528>
- 747 Capitanio, F.A., Stegman, D.R., Moresi, L.N., Sharples, W., 2010. Upper plate controls on deep subduction, trench
748 migrations and deformations at convergent margins. Tectonophysics 483, 80–92.
749 <https://doi.org/10.1016/j.tecto.2009.08.020>

- 750 Chen, Z., Schellart, W.P., Strak, V., Duarte, J.C., 2016. Does subduction-induced mantle flow drive backarc extension?
751 Earth Planet. Sci. Lett. 441, 200–210. <https://doi.org/10.1016/j.epsl.2016.02.027>
- 752 Chertova, M. V., Geenen, T., Van Den Berg, A., Spakman, W., 2012. Using open sidewalls for modelling self-consistent
753 lithosphere subduction dynamics. Solid Earth 3, 313–326. <https://doi.org/10.5194/se-3-313-2012>
- 754 Čížková, H., Bina, C.R., 2013. Effects of mantle and subduction-interface rheologies on slab stagnation and trench
755 rollback. Earth Planet. Sci. Lett. 379, 95–103. <https://doi.org/10.1016/j.epsl.2013.08.011>
- 756 Crameri, F., Tackley, P.J., Meilick, I., Gerya, T. V., Kaus, B.J.P., 2012. A free plate surface and weak oceanic crust
757 produce single-sided subduction on Earth. Geophys. Res. Lett. 39, 1–7. <https://doi.org/10.1029/2011GL050046>
- 758 Dal Zilio, L., Faccenda, M., Capitanio, F., 2018. The role of deep subduction in supercontinent breakup. Tectonophysics
759 746, 312–324. <https://doi.org/10.1016/j.tecto.2017.03.006>
- 760 Dasgupta, R., Mandal, N., 2018. Surface topography of the overriding plates in bi-vergent subduction systems: A
761 mechanical model. Tectonophysics 746, 280–295. <https://doi.org/10.1016/j.tecto.2017.08.008>
- 762 Davies, D.R., Wilson, C.R., Kramer, S.C., 2011. Fluidity: A fully unstructured anisotropic adaptive mesh computational
763 modeling framework for geodynamics. Geochemistry, Geophys., Geosystems 12, n/a-n/a.
764 <https://doi.org/10.1029/2011GC003551>
- 765 Di Giuseppe, E., Van Hunen, J., Funiciello, F., Faccenna, C., Giardini, D., 2008. Slab stiffness control of trench motion:
766 Insights from numerical models. Geochemistry, Geophys., Geosystems 9, 1–19.
767 <https://doi.org/10.1029/2007GC001776>

- 768 England, P.C., Katz, R.F., 2010. Melting above the anhydrous solidus controls the location of volcanic arcs. *Nature* 467, 769 700–703. <https://doi.org/10.1038/nature09417>
- 770 Erdős, Z., Huismans, R.S., Faccenna, C., Wolf, S.G., 2021. The role of subduction interface and upper plate strength
771 on back-arc extension: Application to Mediterranean back-arc basins. *Tectonics* 40, 772 <https://doi.org/10.1029/2021TC006795>
- 773 Faccenna, C., Becker, T.W., Holt, A.F., Brun, J.P., 2021. Mountain building, mantle convection, and supercontinents:
774 Holmes (1931) revisited. *Earth Planet. Sci. Lett.* 564, 116905. <https://doi.org/10.1016/j.epsl.2021.116905>
- 775 Faccenna, C., Becker, T.W., Lallemand, S., Lagabrielle, Y., Funiciello, F., Piromallo, C., 2010. Subduction-triggered
776 magmatic pulses: A new class of plumes? *Earth Planet. Sci. Lett.* 299, 54–68.
777 <https://doi.org/10.1016/j.epsl.2010.08.012>
- 778 Foley, B.J., 2018. On the dynamics of coupled grain size evolution and shear heating in lithospheric shear zones. *Phys.
779 Earth Planet. Inter.* 283, 7–25. <https://doi.org/10.1016/j.pepi.2018.07.008>
- 780 Fowler, C., 2005. *The Solid Earth: An Introduction to Global Geophysics*. Cambridge Univ. Press, Cambridge, U. K.
- 781 Fuchs, L., Becker, T.W., 2021. Deformation memory in the lithosphere: A comparison of damage-dependent weakening
782 and grain-size sensitive rheologies. *J. Geophys. Res. Solid Earth* 126, 1–22.
783 <https://doi.org/10.1029/2020JB020335>
- 784 Fuchs, L., Becker, T.W., 2019. Role of strain-dependent weakening memory on the style of mantle convection and plate
785 boundary stability. *Geophys. J. Int.* 218, 601–618. <https://doi.org/10.1093/gji/ggz167>

- 786 Funiciello, F., Faccenna, C., Giardini, D., 2004. Role of lateral mantle flow in the evolution of subduction systems:
787 Insights from laboratory experiments. *Geophys. J. Int.* 157, 1393–1406. <https://doi.org/10.1111/j.1365->
788 246X.2004.02313.x
- 789 Garel, F., Goes, S., Davies, D.R., Davies, J.H., Kramer, S.C., Wilson, C.R., 2014. Interaction of subducted slabs with
790 the mantle transition-zone: A regime diagram from 2-D thermo-mechanical models with a mobile trench and an
791 overriding plate. *Geochemistry, Geophys. Geosystems* 15, 1739–1765. <https://doi.org/10.1002/2014GC005257>
- 792 Garel, F., Thoraval, C., 2021. Lithosphere as a constant-velocity plate: Chasing a dynamical LAB in a homogeneous
793 mantle material. *Phys. Earth Planet. Inter.* 316, 106710. <https://doi.org/10.1016/j.pepi.2021.106710>
- 794 Gerardi, G., Ribe, N.M., 2018. Boundary Element Modeling of Two-Plate Interaction at Subduction Zones: Scaling
795 Laws and Application to the Aleutian Subduction Zone. *J. Geophys. Res. Solid Earth* 123, 5227–5248.
796 <https://doi.org/10.1002/2017JB015148>
- 797 Gerya, T. V., Connolly, J.A.D., Yuen, D.A., 2008. Why is terrestrial subduction one-sided? *Geology* 36, 43–46.
798 <https://doi.org/10.1130/G24060A.1>
- 799 Gueydan, F., Précigout, J., Montési, L.G.J., 2014. Strain weakening enables continental plate tectonics. *Tectonophysics*
800 631, 189–196. <https://doi.org/10.1016/j.tecto.2014.02.005>
- 801 Gülder, A.J.P., Gerya, T. V., Montési, L.G.J., Munch, J., 2020. Corona structures driven by plume–lithosphere
802 interactions and evidence for ongoing plume activity on Venus. *Nat. Geosci.* 13, 547–554.
803 <https://doi.org/10.1038/s41561-020-0606-1>

- 804 Hall, R., Spakman, W., 2015. Mantle structure and tectonic history of SE Asia. *Tectonophysics* 658, 14–45.
- 805 <https://doi.org/10.1016/j.tecto.2015.07.003>
- 806 Hirth, G., Kohlstedt, D., 2003. Rheology of the upper mantle and the mantle wedge: A view from the experimentalists,
- 807 in: Eiler, J. (Ed.), *Inside the Subduction Factory*. American Geophysical Union, pp. 83–105.
- 808 <https://doi.org/10.1029/138GM06>
- 809 Hirth, G., Kohlstedt, D.L., 1995a. Experimental constraints on the dynamics of the partially molten upper mantle:
- 810 Deformation in the diffusion creep regime. *J. Geophys. Res. Solid Earth* 100, 1981–2001.
- 811 <https://doi.org/https://doi.org/10.1029/94JB02128>
- 812 Hirth, G., Kohlstedt, D.L., 1995b. Experimental constraints on the dynamics of the partially molten upper mantle 2.
- 813 Deformation in the dislocation creep regime. *J. Geophys. Res.* 100, 1981–2001.
- 814 <https://doi.org/10.1029/95jb01292>
- 815 Holt, A.F., Becker, T.W., Buffett, B.A., 2015. Trench migration and overriding plate stress in dynamic subduction models.
- 816 *Geophys. J. Int.* 201, 172–192. <https://doi.org/10.1093/gji/ggv011>
- 817 Holt, A.F., Royden, L.H., Becker, T.W., 2017. The Dynamics of Double Slab Subduction. *Geophys. J. Int.* 209, ggw496.
- 818 <https://doi.org/10.1093/gji/ggw496>
- 819 Huang, Z., Zhao, D., Wang, L., 2015. P wave tomography and anisotropy beneath Southeast Asia: Insight into mantle
- 820 dynamics. *J. Geophys. Res. Solid Earth* 120, 5154–5174. <https://doi.org/10.1002/2015JB012098>
- 821 Kameyama, M., Yuen, D.A., Karato, S.I., 1999. Thermal-mechanical effects of low-temperature plasticity (the Peierls

- 822 mechanism) on the deformation of a viscoelastic shear zone. *Earth Planet. Sci. Lett.* 168, 159–172.
- 823 [https://doi.org/10.1016/S0012-821X\(99\)00040-0](https://doi.org/10.1016/S0012-821X(99)00040-0)
- 824 Karato, S. ichiro, 2010. Rheology of the Earth's mantle: A historical review. *Gondwana Res.* 18, 17–45.
- 825 <https://doi.org/10.1016/j.gr.2010.03.004>
- 826 Király, Á., Capitanio, F.A., Funiciello, F., Faccenna, C., 2017. Subduction induced mantle flow: Length-scales and
827 orientation of the toroidal cell. *Earth Planet. Sci. Lett.* 479, 284–297. <https://doi.org/10.1016/j.epsl.2017.09.017>
- 828 Király, Á., Funiciello, F., Capitanio, F.A., Faccenna, C., 2021. Dynamic interactions between subduction zones. *Glob.
829 Planet. Change* 202, 103501. <https://doi.org/10.1016/j.gloplacha.2021.103501>
- 830 Kramer, S.C., Wilson, C.R., Davies, D.R., 2012. An implicit free surface algorithm for geodynamical simulations. *Phys.
831 Earth Planet. Inter.* 194–195, 25–37. <https://doi.org/10.1016/j.pepi.2012.01.001>
- 832 Kreemer, C., Blewitt, G., Klein, E.C., 2014. A geodetic plate motion and Global Strain Rate Model. *Geochemistry,
833 Geophys. Geosystems* 15, 3849–3889. <https://doi.org/10.1002/2014GC005407>
- 834 Lynch, H.D., Morgan, P., 1987. The tensile strength of the lithosphere and the localization of extension. *Geol. Soc.
835 Spec. Publ.* 28, 53–65. <https://doi.org/10.1144/GSL.SP.1987.028.01.05>
- 836 Lyu, T., Zhu, Z., Wu, B., 2019. Subducting slab morphology and mantle transition zone upwelling in double-slab
837 subduction models with inward-dipping directions. *Geophys. J. Int.* 218, 2089–2105.
838 <https://doi.org/10.1093/gji/ggz268>

- 839 Maruyama, S., Santosh, M., Zhao, D., 2007. Superplume, supercontinent, and post-perovskite: Mantle dynamics and
840 anti-plate tectonics on the Core-Mantle Boundary. Gondwana Res. 11, 7–37.
841 <https://doi.org/10.1016/j.gr.2006.06.003>
- 842 McKenzie, D.P., Roberts, J.M., Weiss, N.O., 1974. Convection in the earth's mantle: towards a numerical simulation.
843 J. Fluid Mech. 62, 465. <https://doi.org/10.1017/S0022112074000784>
- 844 Montési, L.G.J., Hirth, G., 2003. Grain size evolution and the rheology of ductile shear zones: From laboratory
845 experiments to postseismic creep. Earth Planet. Sci. Lett. 211, 97–110. [https://doi.org/10.1016/S0012-821X\(03\)00196-1](https://doi.org/10.1016/S0012-
846 821X(03)00196-1)
- 847 Nakakuki, T., Mura, E., 2013. Dynamics of slab rollback and induced back-arc basin formation. Earth Planet. Sci. Lett.
848 361, 287–297. <https://doi.org/10.1016/j.epsl.2012.10.031>
- 849 Perfit, M.R., Gust, D.A., Bence, A.E., Arculus, R.J., Taylor, S.R., 1980. Chemical characteristics of island-arc basalts:
850 Implications for mantle sources. Chem. Geol. 30, 227–256. [https://doi.org/10.1016/0009-2541\(80\)90107-2](https://doi.org/10.1016/0009-2541(80)90107-2)
- 851 Pindell, J., Kennan, L., Stanek, K.P., Maresch, W. V., Draper, G., 2006. Foundations of Gulf of Mexico and Caribbean
852 evolution: Eight controversies resolved. Geol. Acta 4, 303–341.
- 853 Ranalli, G., 1995. Rheology of the Earth. Springer Science & Business Media.
- 854 Ribe, N.M., 2001. Bending and stretching of thin viscous sheets. J. Fluid Mech. 433, 135–160.
855 <https://doi.org/10.1017/S0022112000003360>

- 856 Romito, S., Mann, P., 2021. Tectonic terranes underlying the present-day Caribbean plate: their tectonic origin,
857 sedimentary thickness, subsidence histories and regional controls on hydrocarbon resources, in: Davison, I., Hull,
858 J.N.F., Pindell, J. (Eds.), *The Basins, Orogenes and Evolution of the Southern Gulf of Mexico and Northern*
859 *Caribbean*. Geological Society of London, p. 0. <https://doi.org/10.1144/SP504-2019-221>
- 860 Ruh, J.B., Tokle, L., Behr, W.M., 2022. Grain-size-evolution controls on lithospheric weakening during continental rifting.
861 Nat. Geosci. <https://doi.org/10.1038/s41561-022-00964-9>
- 862 Santosh, M., 2010. Assembling North China Craton within the Columbia supercontinent: The role of double-sided
863 subduction. *Precambrian Res.* 178, 149–167. <https://doi.org/10.1016/j.precamres.2010.02.003>
- 864 Schellart, W.P., Moresi, L., 2013. A new driving mechanism for backarc extension and backarc shortening through slab
865 sinking induced toroidal and poloidal mantle flow: Results from dynamic subduction models with an overriding
866 plate. *J. Geophys. Res. Solid Earth* 118, 3221–3248. <https://doi.org/10.1002/jgrb.50173>
- 867 Schliffke, N., van Hunen, J., Allen, M.B., Magni, V., Gueydan, F., 2022. Episodic back-arc spreading centre jumps
868 controlled by transform fault to overriding plate strength ratio. *Nat. Commun.* 13, 582.
869 <https://doi.org/10.1038/s41467-022-28228-5>
- 870 Sleep, N.H., Toksöz, M.N., 1971. Evolution of Marginal Basins. *Nature* 233, 548–550. <https://doi.org/10.1038/233548a0>
- 871 Steel, I., Davison, I., 2021. Explanatory note: Map of the geology of the northern caribbean and the greater antillean
872 arc. *Geol. Soc. Spec. Publ.* 504, 1–2. <https://doi.org/10.1144/SP504-2020-3>
- 873 Straub, S.M., Gómez-Tuena, A., Vannucchi, P., 2020. Subduction erosion and arc volcanism. *Nat. Rev. Earth Environ.*

- 874 1, 574–589. <https://doi.org/10.1038/s43017-020-0095-1>
- 875 Suchoy, L., Goes, S., Maunder, B., Garel, F., Davies, R., 2021. Effects of basal drag on subduction dynamics from 2D
- 876 numerical models. *Solid Earth* 12, 79–93. <https://doi.org/10.5194/se-12-79-2021>
- 877 Turcotte, D., Schubert, G., 2014. *Geodynamics*, 3rd ed. Cambridge University Press, Cambridge.
- 878 <https://doi.org/10.1017/CBO9780511843877>
- 879 Uyeda, S., 1981. Subduction zones and back arc basins — A review. *Geol. Rundschau* 70, 552–569.
- 880 <https://doi.org/10.1007/BF01822135>
- 881 Van Benthem, S., Govers, R., Spakman, W., Wortel, R., 2013. Tectonic evolution and mantle structure of the Caribbean.
- 882 *J. Geophys. Res. Solid Earth* 118, 3019–3036. <https://doi.org/10.1002/jgrb.50235>
- 883 Wenker, S., Beaumont, C., 2018. Effects of lateral strength contrasts and inherited heterogeneities on necking and
- 884 rifting of continents. *Tectonophysics* 746, 46–63. <https://doi.org/10.1016/j.tecto.2016.10.011>
- 885 Windley, B.F., Maruyama, S., Xiao, W.J., 2010. Delamination/thinning of sub-continental lithospheric mantle under
- 886 eastern China: The role of water and multiple subduction. *Am. J. Sci.* 310, 1250–1293.
- 887 <https://doi.org/10.2475/10.2010.03>
- 888 Yang, T., Moresi, L., Gurnis, M., Liu, S., Sandiford, D., Williams, S., Capitanio, F.A., 2019. Contrasted East Asia and
- 889 South America tectonics driven by deep mantle flow. *Earth Planet. Sci. Lett.* 517, 106–116.
- 890 <https://doi.org/10.1016/j.epsl.2019.04.025>

